CoCO2
Prototype system for a Copernicus CO_2 service

Impact of System Design on Emission Estimates

Thomas Kaminski, Marko Scholze, Michael Vossbeck, Elise Potier, Grégoire Broquet, Frédéric Chevallier, Tuula Aalto, Aki Tsuruta, Maria Tenkanen, Julia Marshall, Arjo Segers, and Ingrid Super

coco2-project.eu

Co-ordinated by ECMWF

CoCO2

Prototype system for a Copernicus CO_2 service

D5.5 Impact of System Design on Emission Estimates

Dissemination Level:	Public
Author(s):	Thomas Kaminski, Michael Vossbeck (iLab), Marko Scholze (ULUND), Elise Potier, Grégoire Broquet, Frédéric Chevallier (LSCE), Tuula Aalto, Aki Tsuruta, Maria Tenkanen (FMI), Julia Marshall (DLR), Arjo Segers, and Ingrid Super (TNO)
Date:	04/08/2023
Version:	1.0
Contractual Delivery Date:	30/09/2023
Work Package/ Task:	WP5/ T5.5
Document Owner:	iLab
Contributors:	iDLR, FMI, LSCE, TNO ULUND
Status:	Final

CoCO2: Prototype system for a Copernicus CO_2 service

Coordination and Support Action (CSA)
H2020-IBA-SPACE-CHE2-2019 Copernicus evolution – Research activities in support of a European operational monitoring support capacity for fossil CO2 emissions

Project Coordinator: Dr Richard Engelen (ECMWF)
Project Start Date: 01/01/2021
Project Duration: 36 months

Published by the CoCO2 Consortium

Contact:
ECMWF, Shinfield Park, Reading, RG2 9AX,
richard.engelen@ecmwf.int

The CoCO2 project has received funding from the European Union's Horizon 2020 research and innovation programme under grant agreement No 958927.

Table of Contents

1 Introduction

1.1 Background

To support EU countries in assessing their progress for reaching their targets agreed in the Paris Agreement, the European Commission has clearly stated that a way to monitor anthropogenic CO_2 emissions is needed. Such a capacity would deliver consistent and reliable information to support policy- and decision-making processes.

To maintain Europe's independence in this domain, it is imperative that the EU establishes an observation-based operational anthropogenic CO_2 emissions Monitoring and Verification Support (MVS) capacity as part of its Copernicus programme.

The CoCO2 Coordination and Support Action is intended as a continuation of the CO_2 Human Emissions (CHE) project, led by ECMWF. In the Work Programme, ECMWF is identified as the predefined beneficiary tasked to further develop the prototype system for the foreseen MVS capacity together with partners principally based on the CHE consortium.

The main objective of CoCO2 is to perform R&D activities identified as a need in the CHE project and strongly recommended by the European Commission's CO2 monitoring Task Force. The activities shall sustain the development of a European capacity for monitoring anthropogenic CO_2 emissions. The activities will address all components of the system, such as atmospheric transport models, re-analysis, data assimilation techniques, bottom-up estimation, in-situ networks and ancillary measurements needed to address the attribution of CO_2 emissions. The aim is to have prototype systems at the required spatial scales ready by the end of the project as input for the foreseen Copernicus CO_2 service element.

The specific objective of CoCO2 WP5 is to address the role of scales and uncertainty in the MVS.

1.2 Scope of this deliverable

1.2.1 Objectives of this deliverable

The main purpose of Task 5.5 is to assess impact of design options on posterior uncertainty representation.

1.2.2 Work performed in this deliverable

The task has performed data assimilation sensitivity studies and (computationally more efficient) Quantitative Network Desigen (QND) experiments to investigate - where possible in a 'light' and flexible Data Assimilation (DA) system - the impact of different design aspects of the inverse modelling / data assimilation approach on accuracy of the fossil fuel emissions (both best estimate and its uncertainty range).

The DA systems applied in this task span scales from global to regional to local and include

- the global CCFFDAS,
- the local CCFFDAS set up around Berlin,
- Carbon Tracker Europe-CH4 (CTE-CH4),
- The LSCE's Western Europe analytical inversion system, and
- the inverse modelling system LOTOS-EUROS.

1.2.3 Deviations and counter measures

No deviations were encountered.

2 CCFFDAS

2.1 System Description

The Carbon Cycle Fossil Fuel Data Assimilation System (CCFFDAS, Kaminski et al., 2022) pursues an innovative approach to the estimation of fossil fuel emissions in that it combines top-down (inverse modelling) and bottom-up (forward modelling) of sectoral fossil fuel emissions and of the terrestrial biosphere.

With respect to the user requirements identified by CoCO2[1], the CCFFDAS addresses by construction the user requirement of disentangling fossil fuel CO_2 emissions and natural flux. Further, it is worth noting that the system can be operated in two modes. The *synergistic* mode includes (IEA or other) sectoral national emission totals as an observation used in the model parameter calibration. Alternatively, CCFFDAS can be operated in *verification* mode, i.e., without using sectoral national emission totals (typically take from the IEA data base). This latter mode provides emission estimates that are largely independent of data used for the bottom-up estimations of emission, and thus address another user requirement.

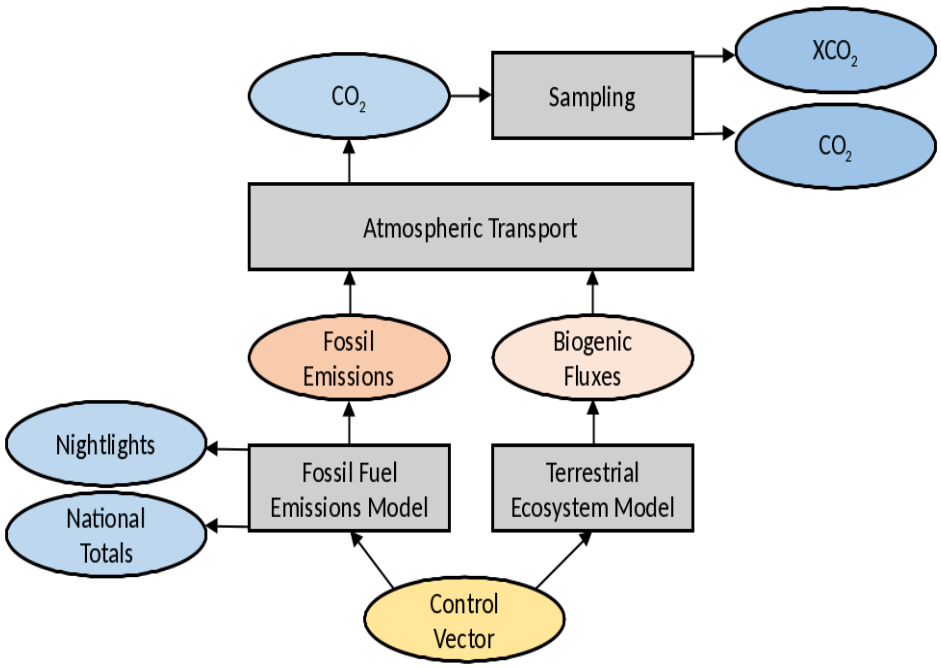

Figure 1. Modelling framework with forward flow of information in CCFFDAS. Boxes represent calculation steps by models, blue ovals observables, and the yellow oval the control vector (model parameters and initial condition)

The (global) CCFFDAS consists of a series of numerical, process-based models simulating the global atmospheric transport of CO_2 (Heimann and Koerner, 2003), the sectoral emissions from fossil fuel usage and the exchange fluxes (photosynthetic uptake and respiratory release) from the terrestrial biosphere (Kaminski et al., 2017). The flow of information in the forward

[1] https://www.coco2-project.eu/sites/default/files/2022-03/CoCO2-D6-3-V1-0.pdf

sense through the modelling chain is shown in Figure 1. The CCFFDAS version used here separates fossil fuel emissions into two sectors, an electricity generation sector and the complement, which is termed other sector (see Asefi-Najafabadi et al., 2014; Kaminski et al., 2022). The electricity generation is simulated per power plant using a prior emission data set per power plant. Emissions from the other sector are simulated by the Kaya identity (Nakicenovic, 2004): the emissions F from the other sector in a 0.1 degree times 0.1 degree gridcell x in country c are given by

$$F(x,c)=pP(x)g(x)ef(c).$$

The variables on the right-hand side are a scalar multiplier, p, for the population density, P(x), a point-wise estimate of the per capita gross domestic product, g(x), a global constant for the energy intensity of the economy, e, and a country-wise estimate for the carbon intensity of energy production, f(c). The output of these models, i.e. the CO_2 fossil fuel emissions (from both the electricity generation and the other sector) and the CO_2 land-atmosphere exchange fluxes, depend on a set of model parameters in the equations (the control vector) used for calculating the fluxes. In the Kaya identity these are denoted by lower case letters and for the electricity generation sector these are the emissions from each listed power station directly. The control vector components for the terrestrial ecosystem model are biome specific parameters controling the photosynthesis and heterotrophic respiration.

For the data sets assimilated into the fossil fuel emission component we refer to Asefi-Najafabady et al. (2014). The terrestrial biosphere component is driven by a data set of Fraction of Absorbed Photosynthetically Active Radiation by plants derived by the Joint Research Centre-Two-stream Inversion Package from satellites (Pinty et al., 2011) and by meteorological data from the fifth generation of ECMWF atmospheric reanalyses of the global climate (Hersbach et al., 2020).

The CCFFDAS operates in two steps:

1. Calibration against observations: The system is used to calibrate these parameters by assimilating the observational data streams. This calibration is based on a Bayesian formalism and uses a variational approach, i.e. a cost function consisting of two terms is minimised iteratively. The first term quantifies the misfit of simulated counterparts to the observational data streams and the second term the deviation to prior estimates of the parameter vector. The minimisation algorithm relies on code for evaluation of the gradient of the cost function with respect to the parameters. This gradient is provided efficiently by the adjoint of the modelling chain. This adjoint is derived by the automatic differentiation tool TAPENADE (Hascoët and Pascual, 2003).

2. Target Simulation: The calibrated model is used to simulate relevant target quantities, i.e. sectoral fossil and biofuel emission fields on a 0.1 degree global grid that are consistent with the observations and the modelling chain.

The estimated sectoral emissions on the 0.1 degree grid resolution can then be aggregated to various territorial units such as national or regional totals. For further details on this global-scale CCFFDAS we refer to Kaminski et al. (2022).

The assessments performed in this study apply the Quantitative Network Design (QND) approach, which is presented in detail by Kaminski and Rayner (2017), see also Tarantola (2005) and Rayner et al. (2019). In brief, it performs a rigorous uncertainty propagation from the observations to a target quantity of interest relying on the indirect link from the observations to the target variables established by a numerical model. The link has to be indirect, because, in general there is no direct link from the observations to the target quantity. There are, however, direct links from the control vector, which includes the uncertain inputs to the

modelling chain, to target quantities and observations (the two steps of operator described above).

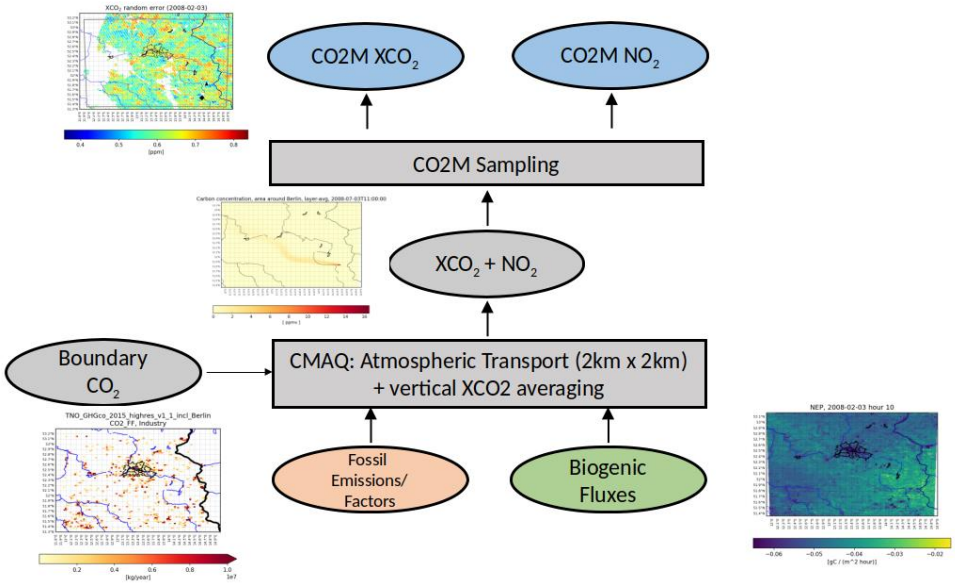

Figure 2: The flow of information in the forward sense through the modelling chain of the local CCFFDAS. Boxes represent calculation steps by models, blue ovals observables, and the orange and green ovals the control vector (model parameters).

For some of the experiments conducted here, we used a local setup of the CCFFDAS. As the system is described in the published literature we focus our description on the aspects that are particularly relevant for this study and refer for more detail to Kaminski et al. (2022b).

The local CCFFDAS is built around a modelling chain to simulate two CO2M XCO2 satellite images over the Berlin area, one on 3 February 2008 and one on 3 July 2008, starting 24 h before the respective acquisitions. The flow of information in the forward sense is shown in Figure 2. As in the global CCFFDAS, the CO2M observation impact is assessed through the QND approach, which is based on a representation of the modelling chain through a Jacobian matrix that quantifies the sensitivity of the measurements as a function of the control vector. Our control vector consists of the surface emissions into each grid cell and the lateral inflow of CO_2 as well as scaling factors of the NO_2/CO_2 emission ratio. Our 24 h simulation period is sufficiently long to ensure that the initial concentration has left our 200 × 200 km^2 domain under typical wind conditions, i.e., we can safely ignore it in the control vector.

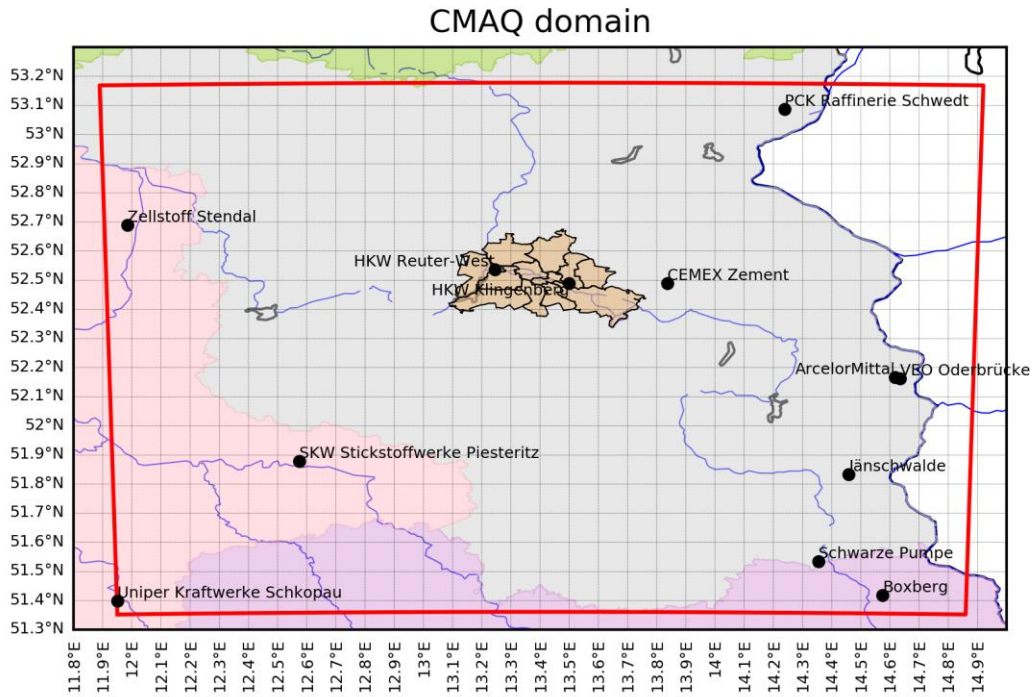

Figure 3: Model domain including the locations of the largest emitting power plants.

To link the emission models to XCO2 and NO_2 observations by CO2M we use version 5.2.1 of the Community Multiscale Air Quality model (US EPA Office of Research and Development, 2018), which can be run as an offline tracer transport model with meteorological input fields derived from the Weather and Research Forecast model (WRF, version 3.9.1.1, (Skamarock et al. 2008). Our model domain of 200 km by 200 km around Berlin is shown in Figure 3. Over this domain we operate the model at a horizontal resolution of 2 km by 2 km with 32 vertical layers.

For the time scales addressed in the present study, CO_2 is considered chemically inert. By contrast, the loss of NO_2 due to chemical processes needs to be taken into account. The model achieves this through an atmospheric lifetime. For the summer case we use a lifetime of 4 h and for the winter case we regard also NO_2 as inert.

Name	fuel type	CO2 emission [MtC/yr]	NO2/CO2 emission ratio
LEAG, Kraftwerk Jänschwalde	solid	6.48	0.0029
Kraftwerk Boxberg	solid	5.33	0.0025
LEAG, Kraftwerk Schwarze Pumpe	solid	3.36	0.0017
Uniper Kraftwerke GmbH (Schkopau)	solid	1.46	0.0024
PCK Raffinerie GmbH Schwedt	liquid	0.87	0.0025
ArcelorMittal Eisenhüttenstadt GmbH	gaseous	0.72	0.0018
Vattenfall Europe Wärme HKW Reuter-West	solid	0.59	0.0030
SKW Stickstoffwerke Piesteritz GmbH	solid	0.59	0.0008
VEO Vulkan-Energiewirtschaft - Oderbrücke GmbH	gaseous	0.46	0.0001
CEMEX Zement GmbH	solid	0.39	0.0036

Table 1: Fuel type, annual CO2 emissions, and NO2/XCO2 emission ratio for the 10 power plants in the domain with highest CO2 emissions.

For the electricity generation sector we take the locations of power plants, temporal emission profiles, as well as annual emissions of CO_2 and NOx from a data set (Super et al. 2020) compiled as part of the European commission's CHE project (Balsamo et al. 2021). Table 1 shows the relevant characteristics of the 10 largest power plants in the domain with highest CO_2 emissions. The control vector for the electricity generation sector consists of the CO_2 emission of each power plant and of a scaling factor for the NO_2 to CO_2 emission ratio, which also absorbs uncertainties in the NO_2 to NOx ratio. Prior uncertainties of the CO_2 emission are assumed to be a constant fraction of 20% of the emission. With regard to the degree of differentiation of the scaling factor of the NO_2/XCO2 emission ratio we explore three cases:

- Uniform: All plants in our domain share the same scaling factor.
- Per type: All plants in our domain of the same fuel type share the same scaling factor.
- Per plant: Each plant in our domain has an individual scaling factor.

fuel type	σ
solid	0.098
liquid	0.245
gaseous	0.924
average	0.422

Table 2: 1 sigma uncertainty range in the NO2 to CO2 emission ratio for each fuel type.

The prior value for the scaling factor is 1. The (relative) prior uncertainty of the emission factor ratio is calculated from reported emission factor uncertainties averaged for several countries, following the approach used by (Super et al. 2020), see Table 2.

Our “other” sector accounts for fossil fuel emissions from all sectors except electricity generation. Other sector emissions of CO_2 and NOx are also taken from the data set by (Super et al. 2020). As the "other" sector includes several processes, the resulting emission ratio varies spatially depending on the contributions of different processes. The control vector for the other sector consists of the CO_2 emission into each model grid cell and of a scaling factor for the NO_2 to CO_2 emission ratio. In our experiments, we use a (spatially uncorrelated) prior uncertainty of 52.8% of the emissions into a grid cell for each grid cell, which translates to a 20% prior uncertainty when aggregated over Berlin. For the scaling factor of the NO_2/CO_2 emission ratio we use a prior of 1 and the prior uncertainty for the average over fuel types.

The terrestrial biosphere model we used to calculate the natural terrestrial CO_2 exchange fluxes is based on the Simple Diagnostic Biosphere Model (SDBM, Knorr et Heimann, 1995), which was used by Kaminski et al. (2012) for assimilation of CO_2 and by (T. Kaminski et al. 2017) for assimilation of XCO2. Here we use a new implementation (Kaminski et al. 2022b) on the 2 km by 2 km grid of the transport model with a time step of 1 hour. It calculates the uptake of CO_2 by photosynthesis (expressed as Gross Primary Productivity, GPP) using a light-use efficiency approach and ecosystem respiration using a temperature dependency. The control vector consists of 5 parameters that were calibrated against a set of eddy-covariance sites. We use a prior uncertainty range of 20% for each of the parameters.

For our experiments with the local CCFFDAS, the control vector is composed of the fossil fuel emissions from power plants, the fossil fuel emissions from the other sector, the inflow from the boundary, scaling factors for the NO_2/CO_2 emission ratio, and the parameters of the terrestrial biosphere model.

The target quantities are fossil fuel emissions for each power plant and from the other sector on the 2 × 2 km2 pixel scale and aggregated to larger scales, including the scale of Berlin districts and of the entire city. The observational impact on the target quantities is quantified by the above-described two-step procedure: The first step uses the observational information

to reduce the uncertainty in the control vector, i.e., from a prior to a posterior state of information. The second step propagates the posterior uncertainty forward to the simulated target quantity.

Each CO2M satellite has a repeat cycle of 11 days. We apply our QND framework around the CCFFDAS to the simulated uncertainty in single measurement retrievals of CO2M for two specific overpasses with low cloud cover over our study domain around Berlin, one in winter and one in summer. Random and systematic errors were estimated from an error parameterisation formula that exploits the availability of aerosol information from a multi-angular polarimeter (MAP) onboard each CO2M satellite. We computed the variance of the XCO2 observational uncertainty as the sum of the variances of random and systematic errors. This reflects the assumption that systematic and random errors are independent of each other and also in space.

For the retrieval uncertainty in tropospheric column NO_2 we follow the estimates of Lorente et al., 2019 for the TROPOMI NO2 retrieval. For the random uncertainty we use their estimate of the slant column error for the TROPOMI retrieval, which is $0.5–0.6 \cdot 10^{15}$ molec cm^{-2}. We use a systematic error of $0.3 \cdot 10^{15}$ molec cm^{-2}. We regard random and systematic error as independent and compute the variance of the NO_2 observational uncertainty as the sum of the variances of random and systematic errors. We will also investigate the sensitivity of the posterior uncertainties with respect to the uncertainty in NO_2.

The inflow from the lateral boundary is represented in the control vector by one component for each group of 5 grid cells in the horizontal at each of the vertical levels with prior uncertainty of 0.53 g(C)/day.

2.2 Analyses and Conclusions

Following a request by the CO2M mission task force, we applied the global CCFFDAS in a study that assessed for an exemplary week in June posterior uncertainties in sectoral fossil fuel emissions at country scale for five selected countries (see Figure 4) expressing the constraints from several observational scenarios ranging from small in situ networks providing continuous CO_2 measurements to synthetic observations from constellations of one to four CO2M satellites.

The study reveals that each additional satellite in the constellation achieves a further reduction in posterior uncertainty of country scale sectoral fossil fuel emissions. As the electricity generation sector is relatively well-constrained by prior information, at country scale the main impact of atmospheric (X)CO_2 observations was on the posterior uncertainties of the fossil fuel emissions from the other sector. For example, extending the constellation from one to four satellites reduces the posterior uncertainty of fossil fuel emissions from China's other sector from ~180 MtC/yr to 124 MtC/yr, i.e. by roughly 30%. The added value of an extra satellite varies depending on the country and the local conditions (e.g., cloud cover) during the study week. For three out of the five countries the third satellites brings the largest added value in terms of reduction in posterior uncertainty. For Germany, adding the second satellite reduces the posterior uncertainty of the other sector by ~2%, while adding the third satellite to the constellation reduces the posterior uncertainty of the other sector by another ~16%. The study also explored whether a two-satellite CO2M constellation with increased swath width (350 km instead of 250 km) and reduced precision (0.9 ppm instead of 0.7 ppm) could achieve a performance similar to the three-satellite configuration with 250 km swatch and 0.7 ppm precision. This was not the case: Even though the two-satellite CO2M constellation with increased swath width (350 km instead of 250 km) and reduced precision (0.9 ppm instead of 0.7 ppm) has marginally better performance than the nominal 2 satellite configuration (i.e. better spatial coverage overcompensates slightly for the performance loss through lower precision) it is still much inferior to the three satellite configuration. Even in comparison with

the case of a single satellite, the performance of in situ networks of varying sizes is much weaker (Kaminski et al., 2022).

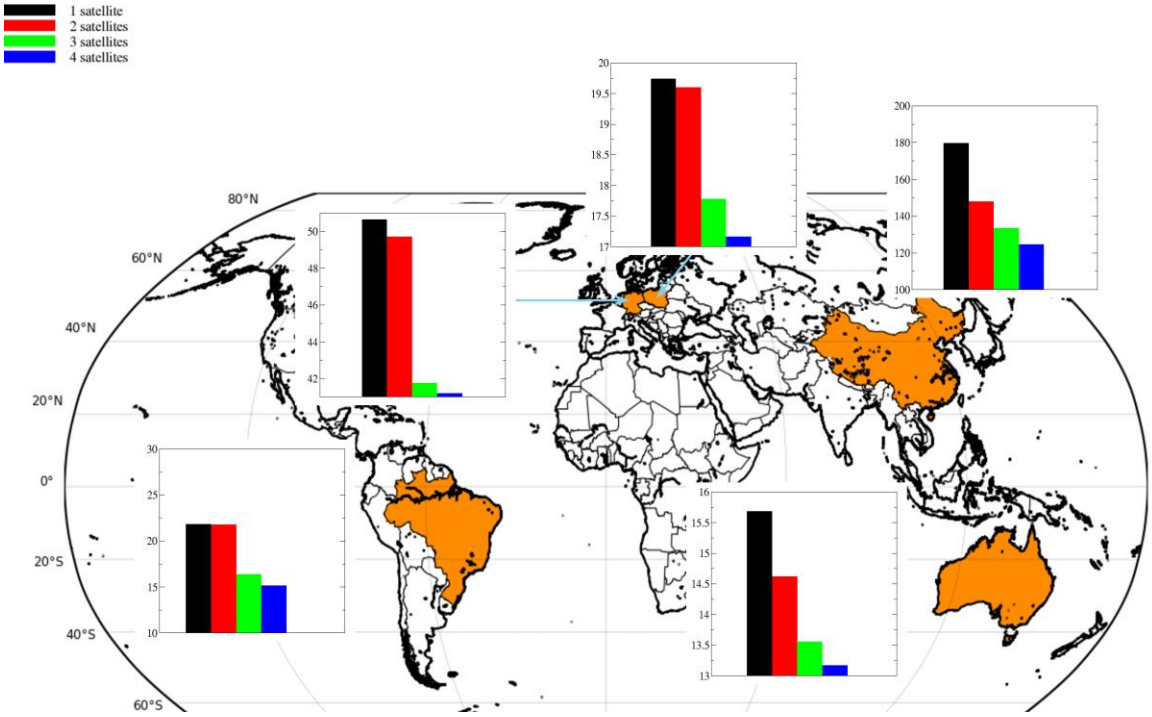

Figure 4: Estimated uncertainty in annual emission rates in MtC/yr for Australia, Brazil, China, Germany and Poland, and for various assumed CO2M constellations providing observations over land only (nadir view). Main focus should be on results from 2 satellites (red) versus 3 satellites (light green) with a 250 km swath width.

#	Name	XCO_2	NO_2
1	EPFMAP (default)	NN w/MAP	—
2	PMIF	PMIF	—
3	EPF	NN w/o MAP	—
4	NO_2 uniform	NN w/MAP	σ_r uniform
5	NO_2 per type	NN w/MAP	σ_r per fuel type
6	NO_2 per plant	NN w/MAP	σ_r per plant
7	1/2 plant prior σ	NN w/MAP	—

Table 3: Initial set of experiments with local CCFFDAS.

A further series of seven experiments applied the local CCFFDAS, and is listed in Table 3. Experiments 1-3 and 4 assimilate XCO2 only, while experiments 4-6 add complementary NO_2 observations. The latter explore the three above-defined cases with regard to the degree of differentiation of the scaling factor of the NO_2/XCO2 emission ratio. Experiments 1 and 3-7 assume XCO2 retrievals benefit form complementary aerosol observations provided by the MAP, while Experiment 3 excludes that information. Experiment 2 relies on an alternative hypothetical XCO2 product (Buchwitz et al., 2013). Each of the seven experiments was

conducted for a day in winter and a day in summer. For further detail we refer to Kaminski et al. (2022).

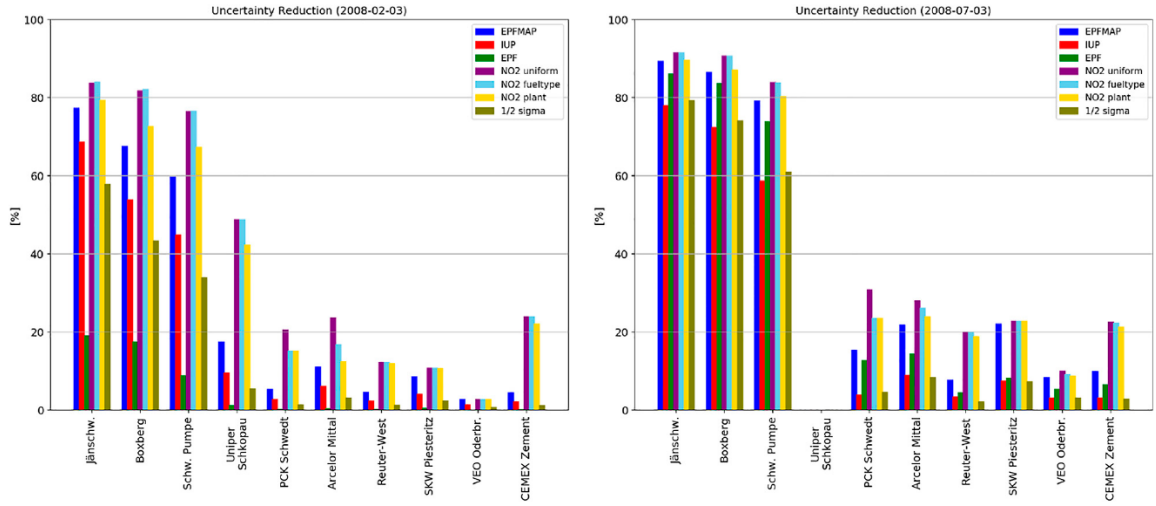

Figure 5: Uncertainty reduction for ten largest power plants and all experiments in winter (left) and summer (right).

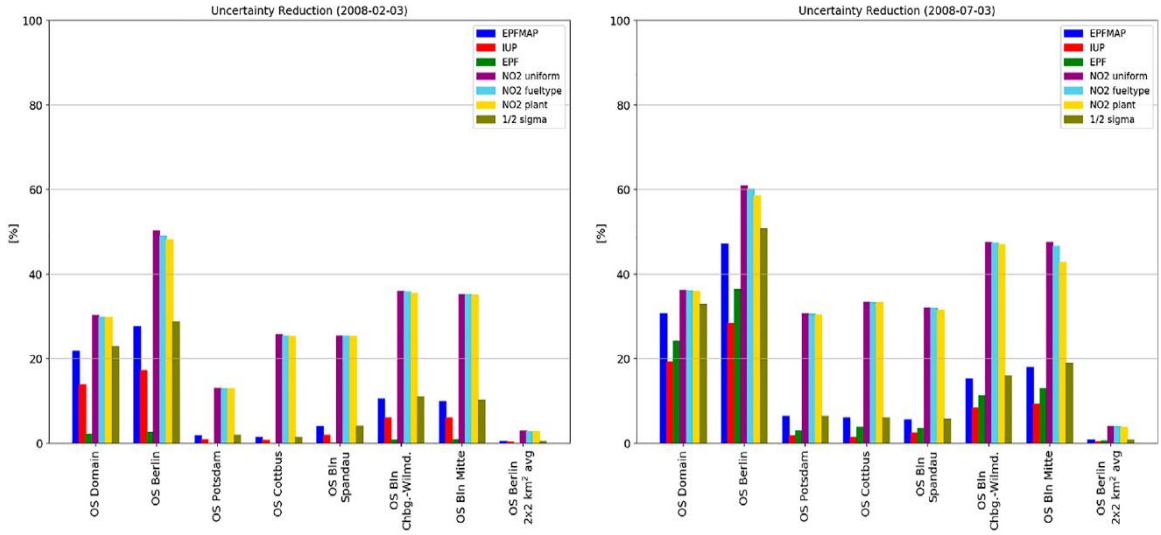

Figure 6: Uncertainty reduction for the other sector at spatial scales from entire domain to grid cell and all experiments in winter (left) and summer (right).

In Experiment 1, a large uncertainty reduction (≈60%–90%) is found for the three largest power plants and a moderate uncertainty reduction (up to 10%–20%) for the next largest (Figure 5). The uncertainty reduction is higher in the summer case, when both random and systematic errors are lower. The plant in Schkopau is a special case as it is covered by clouds in both periods. Due to its location on the western boundary in combination with easterly winds in the winter case its plume is not observed over our domain in that period.

Next, we present uncertainty reductions for the other sector on the scales of the 2 km by 2 km grid cells, aggregated over Berlin districts, over the entire city, over some other towns in the domain, and over the entire domain (Figure 6). As for the power plants, the uncertainty reduction is considerably larger in the summer case. While the uncertainty reduction is low (up to 4% in the winter case and 8% in the summer case) at the grid cell scale and focuses on grid cells with higher emissions, it increases for emissions accumulated to the Berlin district scale (up to about 10% in the winter case and 20% in the summer case) and is higher for

districts with higher emissions (not shown). At the scale of Berlin we see a sizeable uncertainty reduction (about 28% in the winter case and 47% in the summer case).

Experiment 4 adds NO_2 measurements to the default setup (experiment 1). The extra NO_2 measurements increase the uncertainty reduction for the large power plants (Figure 5) in the summer and winter cases. In relative terms the increase in uncertainty reduction is particularly high for the plants which were not well observed with XCO2 alone and those with high NO2/CO2 emission ratio.

The absolute reduction in posterior uncertainty through the addition of the NO_2 measurements is, however, highest for the larger power plants. In relative terms the increase in uncertainty reduction is higher in the winter case, when the constraint by XCO2 alone is weaker. The best overall performance of XCO2 and NO_2 is, however, achieved in the summer case, when both random and systematic errors are lower. Likewise for the other sector, the extra NO_2 measurements increase the uncertainty reduction on all scales in the summer and winter cases. On the grid cell scale uncertainty reductions reach now 25% in the winter case and 40% in the summer case. High values reflect the combination of high emission ratio with high CO_2 emissions. On the Berlin district scale the relative increase in uncertainty reduction is particularly high for districts that were not well constrained by XCO2 alone such as Spandau. In absolute terms the posterior uncertainty decreases most for districts with larger emissions such as Charlottenburg-Wilmersdorf. With the extra NO_2 measurements the uncertainty reduction in the other sector emissions aggregated over Berlin increases to about 50% in the winter case and 60% in the summer case. The best overall performance of XCO2 and NO_2 for the other sector is achieved in the summer case.

Figure 5 shows the uncertainty reduction for the 10 largest power plants and all experiments of the winter (left) and the summer (right) periods. The default experiment performs better than the experiment 2 for all power plants, reflecting the lower random and systematic errors of the default case. The MAP improves the impact of the CO2M measurements for all power plants and in the summer and winter cases. Over our study domain, the impact of the MAP is particularly high in the winter case. Even with reduced prior uncertainty there is strong uncertainty reduction for large power plants, in particular in the winter case, when XCO2 alone leaves more scope for improvement and the atmospheric NO_2 lifetime is longer. The differentiation of the scaling factors in the NO_2/CO_2 emission ratio has an impact on the uncertainty reduction. As expected, a uniform scaling factor yields higher uncertainty reduction than a scaling factor per plant. This is because the uniform scaling factor is constrained by the atmospheric observations of all plants (transfer of information between plants), while an independent plant-specific scaling factor is only constrained by the atmospheric observations of the plant in question. In other words, the case of the uniform scaling factor imposes more prior knowledge as it removes the independence of the scaling factors. In between these two cases lies the case with a scaling factor per fuel type, with the exception of the largest of the ten power plants where it outperforms the case with uniform scaling factor. The four largest plants belong to the type burning solid fuel, for which there are two competing effects when changing from the case “uniform” to the case “fuel type”. First, the prior uncertainty in the emission ratio for solid fuel is considerably lower than the average we use in the uniform case, which increases the performance of the NO_2 measurements. Second, the transfer of information from one power plant to the next through the use of the same scaling factor for the emission rate is obviously weaker in the case “fuel type” than in the case “uniform”, because the information is shared between fewer power plants. For the larger plants the first effect dominates the second. In the winter case this concerns the first four power plants and in the summer case the first two.

Figure 6 shows the uncertainty reduction for the other sector at spatial scales from the entire domain to grid cell and all experiments in the winter (left) and the summer (right) periods. The default case performs better than experiment 2 over all scales. The MAP improves the impact of the CO2M measurements over all scales and in the summer and winter cases. Over our study domain, the impact of the MAP is particularly high in the winter case. Increasing the

differentiation of the scaling factor for the NO_2/CO_2 emission ratio of the power plants (from experiment 4 to experiment 5 to experiment 6) yields a slight decrease of the performance of the other sector.

This is a typical example demonstrating a general feature of the CCFFDAS, namely that, through the atmospheric constraint, better prior information (same emission ratio between power plants) on one sector (here electricity generation) is translated to better information on the remaining sectors (here the other sector). Similarly, the reduced prior uncertainty for the power plants (experiment 7), yields a slight performance increase for the other sector.

We summarise the results of the seven experiments as follows: We find that XCO2 measurements alone provide a powerful constraint on emissions from larger power plants and a constraint on emissions from the other sector that increases when aggregated to larger spatial scales. The MAP improves the impact of the CO2M measurements for all power plants and for the other sector on all spatial scales. Over our study domain, the impact of the MAP is particularly high in the winter case. NO_2 measurements provide a powerful additional constraint on the emissions from power plants and from the other sector. Through the atmospheric constraint, more prior information on the CO_2 emissions from power plants or on the differentiation of the NO_2/CO_2 emission factor reduces the uncertainty in CO_2 emissions from the other sector.

Our results suggest that the capability of CO2M measurements to constrain fossil fuel emissions varies between summer and winter cases. The main factor behind the larger constraint in the summer case are lower random and systematic errors in XCO2 measurements. There are, however, exceptions related to factors such as cloud cover and atmospheric transport. The setup of the CCFFDAS and of the experiments focus on specific uncertain elements in the processing chain and its inputs.

Further uncertain factors such as structural model errors are not covered, so that the quantitative assessments with the current prototype might be interpreted as a lower limit for posterior uncertainty. We can, however, expect that, with sufficient research effort, future CCFFDAS's will be able to benefit from more accurate models of fossil fuel emissions (finer sectoral resolution, further observational constraints), of natural fluxes (more terrestrial observations including CO2M measurements of solar induced fluorescence, better meteorological driving data), and of atmospheric transport (constrained by observations of local meteorological conditions) and improved prior information. In this sense our performance assessments may provide a realistic indication of what can be achieved. In summary we find that the combination of CO2M with a suitable inversion system can provide useful estimates for urban scale emission reporting/verification. As for the above described global CCFFDAS (Kaminski et al., 2022), possible application modes are either a verification mode, in which the system is operated largely independently from inventory information or a synergy mode that derives a best emissions estimate by integrating bottom up information.

In a further set of experiments we used the local CCFFDAS to explore the added value provided by a co-emitted species, namely NO_2 and the effect of the random error in the NO_2 retrieval. Figures 7-9 show the following 4 cases (systematic error in all cases 0.3 10^{15} molec/cm^2):

- No NO_2 (above Experiment 1)
- Random error 0.5 10^{15} molec/cm^2 (Lorente et al., 2019; above Experiment 4),
- Random error 1.5 10^{15} molec/cm^2 (upper limit specified in the mission requirements document)
- Random error 0.25 10^{15} molec/cm^2

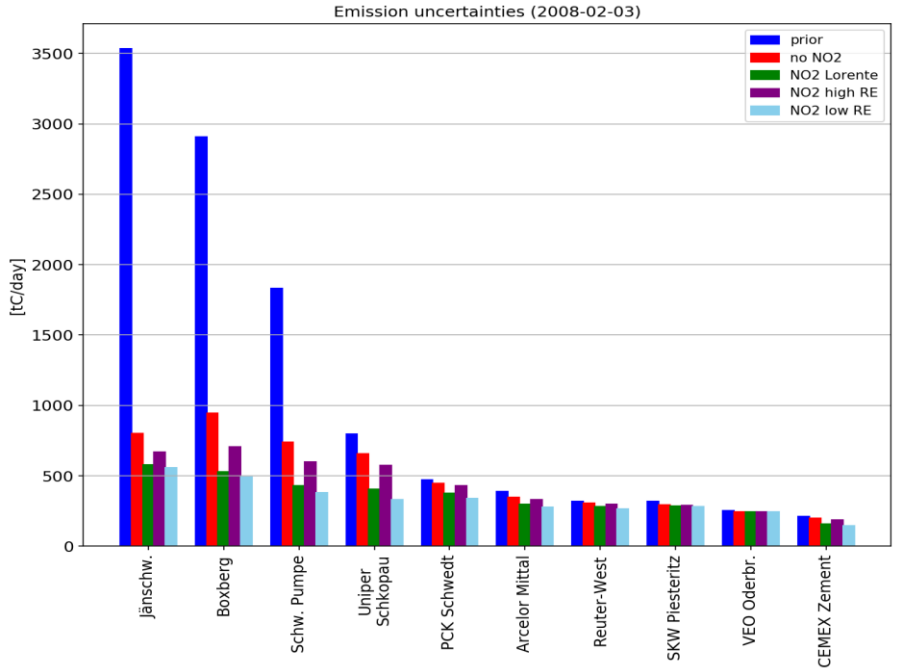

Figure 7: Uncertainty for the 10 largest power plants in domain

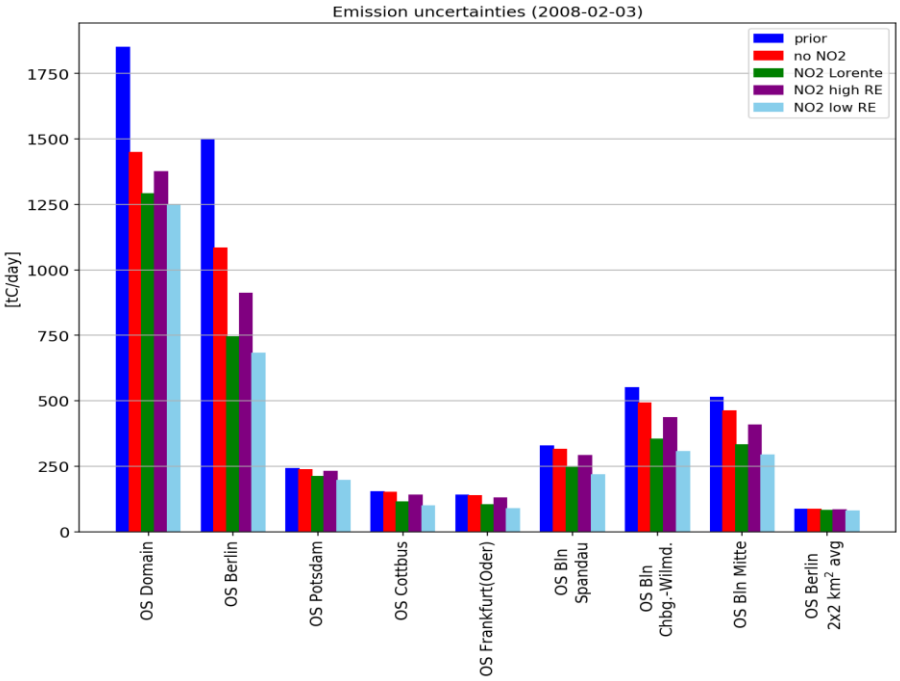

Figure 8: Uncertainty for emissions from other sector (complement of electricity generation sector) for scales from domain, to city to district, to grid cell.

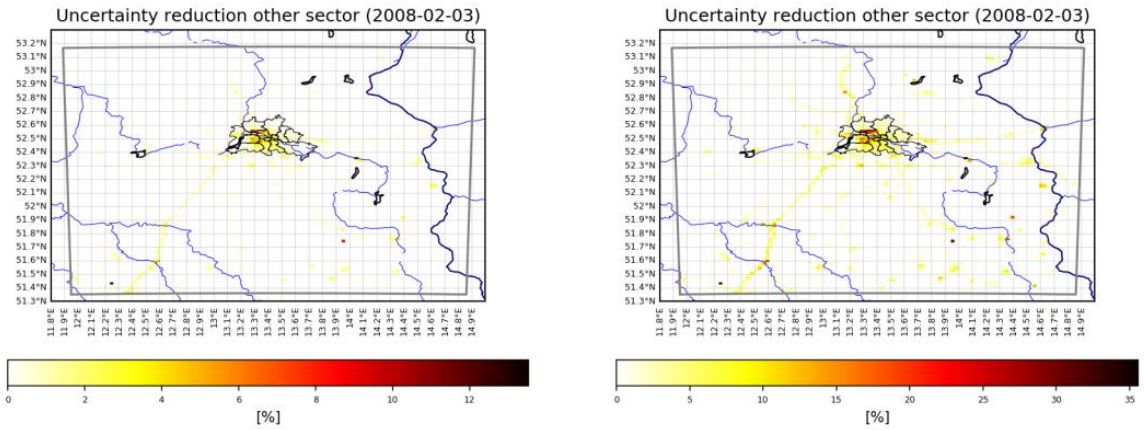

Figure 9: Uncertainty for emissions from other sector (complement of electricity generation sector) for case without (left) and with (right) NO_2 random error 0.5 10^{-15} molec/cm^2.

The impact of the random error in NO_2 observations (Figures 7-9) can be summarised as follows:

- NO_2 still useful when random error is tripled
- Reduction in NO_2 random error (to level just below that of systematic error) yields a small benefit (extra uncertainty redution of ~10% at city scale).

We note that in addition to the assessments presented here, WP4.3 used the local CCFFDAS to assess the impact of the domain boundary on the posterior emission uncertainty.

3 Carbon Tracker Europe-CH4

3.1 System Description

Carbon Tracker Europe – CH4 (CTE-CH4) is an atmospheric inverse model that optimizes global surface CH4 emissions region-wise based on an EnKF (Evensen, 2003) used to minimize a cost function:

$$J = \left(x - x^b\right)^T P^{-1}\left(x - x^b\right) + \left(y - H(x)\right)^T R^{-1}\left(y - H(x)\right), (eq.1)$$

where x (dimension N) is a state vector that contains a set of scaling factors that multiply the CH4 surface emissions (E) that we wish to optimize, starting from a prior estimate of these emissions (E^b) and scaling factors x^b. P is the covariance matrix of the state vector, y is a vector of atmospheric XCH4 observations, R is a covariance matrix of the observations y, and H is an observation operator. In the basic set-up, the cost function in Eq. (1) is minimized using an EnKF with 500 ensemble members. The TM5 chemistry transport model (Krol et al., 2005) is used as an observation operator that transforms emissions E into simulated atmospheric $\mathrm{XCH4}$ $(H(x))$. The emissions E are optimized weekly, with an assimilation window smoother length (lag) of 5 weeks. Anthropogenic and biospheric emissions are optimized, while emissions from other sources (fire, termites, and oceans) are not optimized. The optimal weekly mean CH4 fluxes (F_{tot}), in region r and time (week) t, are calculated as follows:

$$F_{tot}(x,y,t) = \lambda_b(x,y,t) \cdot F_{bio}(x,y,t) + \lambda_a(x,y,t) \cdot F_{anth}(x,y,t) + F_{oce}(x,y,t) + F_{fire}(x,y,t) + F_{term}(x,y,t), (eq.2)$$

where F_{bio}, F_{ant}, F_{fire}, F_{term}, F_{oce}, are the prior emissions from the biospheric, anthropogenic activities, fire, termites and oceans, respectively. CTE-CH4 optimizes the scaling factors λ so that CH4 fluxes from anthropogenic and biospheric sources are solved simultaneously. The fluxes from other sources are not optimized. The spatial optimization resolution varies from 1° x 1° (latitude x longitude) to 6° x 4°, depending on the chosen inversion set-up. The highest 1° x 1° optimization resolution is typically applied to Northern High Latitudes (>50°N) and Europe. The anthropogenic and biospheric sources are assumed independent, and the uncertainty of the prior fluxes over land is assumed to be 80% and 20% over oceans. The spatial correlation length varies in land areas from 100 km to 500km (ocean 900 km) between optimization regions based on the grid/optimization region size and observation density. For the regions where fluxes are optimized at 1° x 1° resolution, correlation length is 100 km. We apply no prior correlation on temporal dimensions.

Prior Emissions

Prior emissions include biospheric, anthropogenic, fire, termites and ocean sources and these are taken from process-based models and inventory data. For biospheric fluxes, we use the estimates from LPX-Bern DYPTOP v1.4 model (Lienert et al., 2018) and the ensemble of Global Carbon Project models (Saunois et al., 2020). For other a priori sources, we used estimates from EDGAR v6.0 (Crippa et al., 2020) for anthropogenic, GFED v4.2 (Giglio et al., 2013) for fire, VISIT (Ito et al., 2012) for termites, geological sources (scaled to 23 Tg CH4 /yr) from Etiope et al (2019) and ocean sources from Weber et al (2019).

Atmospheric observations

CH4 fluxes are constrained with atmospheric methane mole fraction data mainly from the Integrated Carbon Observation System (ICOS), NOAA ObsPack v2.0 and World Data Center for Greenhouse Gases (WDCGG) which contains data from global in situ stations. In addition, we add the northern high latitudes (NHL) observations from in situ stations of Finnish Meteorological Institute (FMI), National Institute for Environmental Studies (NIES), and Max Planck Institute for Biogeochemistry (MPI-Biogeochemistry). The data contains both weekly discrete air samples and hourly continuous measurements. The hourly data is pre-processed before inversion by taking daily averages similarly to Tsuruta et al. (2017). The observation uncertainties are defined for each site and observation based on site characteristics and

measurement accuracy. The observation uncertainty includes also information about TM5's ability to reproduce the mole fractions. During the assimilation process, if the absolute differences between observations and prior mole fractions are larger than 30 ppb, the observations are rejected, i.e. not assimilated to constrain the fluxes.

For inversions with TROPOMI data two retrieval products are used: SRON operational product (OPER) and University of Bremen WFMD research data (WFMD). Both data are pre-processed to 1° x 1° daily resolution by taking median XCH4 of the grid as the observation. For the calculation of the averaging kernel, the prior XCH4 and profile information is taken from the sounding which has closest XCH4 value to the daily median. The observational uncertainties are calculated as aggregation errors + transport model errors. The aggregating errors are calculated as the standard deviation of XCH4 values in 1° x 1° in the daily grid. The minimum aggregation error is set as 5 ppb. The transport model error is set as a globally uniform value of 15 ppb, i.e., the minimum observational uncertainty is theoretically 20 ppb.

3.2 Analyses

3.2.1 Uncertainty estimates in ground-based and satellite inversions

FMI studied the impact of the inversion set-up on the posterior flux uncertainty estimates in connection to assimilation of satellite and ground-based surface observations of methane into the Carbon Tracker Europe – CH4 (CTE-CH4) atmospheric inversion model. Satellite and surface observations are significantly different in terms of number of data and its uncertainties, and the distribution of data in spatial and temporal domains, which calls for re-assessment of the inversion set-up. The CTE-CH4 simulations were carried out for year 2018 using three sets of atmospheric data: (1) TROPOMI WFMD data (InvWFMD), (2) TROPOMI OPER data (InvOPER) and (3) ground-based surface data (InvSURF). In TROPOMI inversions InvWFMD and InvOPER, only the satellite data are assimilated. In addition, assimilation window tests were made in a simple pointwise application to test multiple parameter combinations. Further, a new set of prior flux uncertainties was tested in a global inversion utilising surface observations.

3.2.1.1 Impact of assimilation window

Two temporal sequences are used in CTE-CH4 in connection to data assimilation by EnKF; the flux optimisation window and lag window, lag smoothing the flux result and ensuring that the signals of sources further away in time from the observing sites are included in the analysis. The length of lag-window defines the information content in the observations in the temporal dimension, and therefore, the influence of the size of the lag window in connection to different types of observations could be relevant, especially when considering short temporal changes. However, in the TROPOMI vs surface inversion work we considered the differences in observation data intensity through testing of the size of the flux optimisation window, and the size of the lag window was calculated following earlier approaches as multiplication of the size of the flux optimization window. We applied the flux optimisation window of three days for the inversions using the TROPOMI data and seven days for the inversion using the surface data. The EnKF lag-multiplier of five was employed for both, i.e., the lag-window is 15 days for the TROPOMI inversions and five weeks for the surface inversion. A shorter flux optimisation window was applied in the TROPOMI case as the number of data points was significantly larger in TROPOMI data compared to surface data. Sufficient number of data points is needed to be assimilated for each time step, but the number should be

limited to some extent to make the simulations computationally feasible. We found that in inversions with the TROPOMI satellite data the flux uncertainty reduction was in annual-to-monthly scales comparable to the in-situ inversion, in which we used the longer assimilation window. These results are presented in Tsuruta et al. (2023).

We also made some tests for the flux optimization window and EnKF lag window in a computationally light set-up, testing the EnKF in simplified pointwise application of the full CTE-CH4 global system. The aim here was to learn about and develop the system towards more efficient utilization of locally measured data at an ICOS supersite. Methane observations at the Hyytiälä tall tower, located in the boreal forest and wetland region with rural settlements, were assimilated into the model system, where prior fluxes, background and assimilation routines were adopted from the global set-up. Both anthropogenic and biospheric fluxes were optimized. An ensemble size of 800 was used in the lag and flux optimisation window tests, since uncertainty of the state estimate was reduced from prior to posterior and variability in the posterior estimates reduced with larger ensembles. In the tests, the ratio of posterior state variance to prior state variance (δ_{UNC}) was solved for a period of four years for the biospheric and anthropogenic flux components. δ_{UNC} values smaller than one indicate a reduction in uncertainty of the state.

The size of the flux optimisation window varied from 4 to 19 days, and these sizes were multiplied with lag values ranging from 2 to 11 to obtain the lag-window (Figure 10). Longer windows seemed to reduce δ_{UNC} more than shorter windows, but the results should not be interpreted as giving general advice on choice of the length of the assimilation window. The results may be related more to the configuration of the atmospheric background and prior sources, and choices of other inversion parameters and prior uncertainties in the pointwise application rather than to the choice of the length of the assimilation window. Further studies are needed on the topic, both using the computationally light set-up and the full global system.

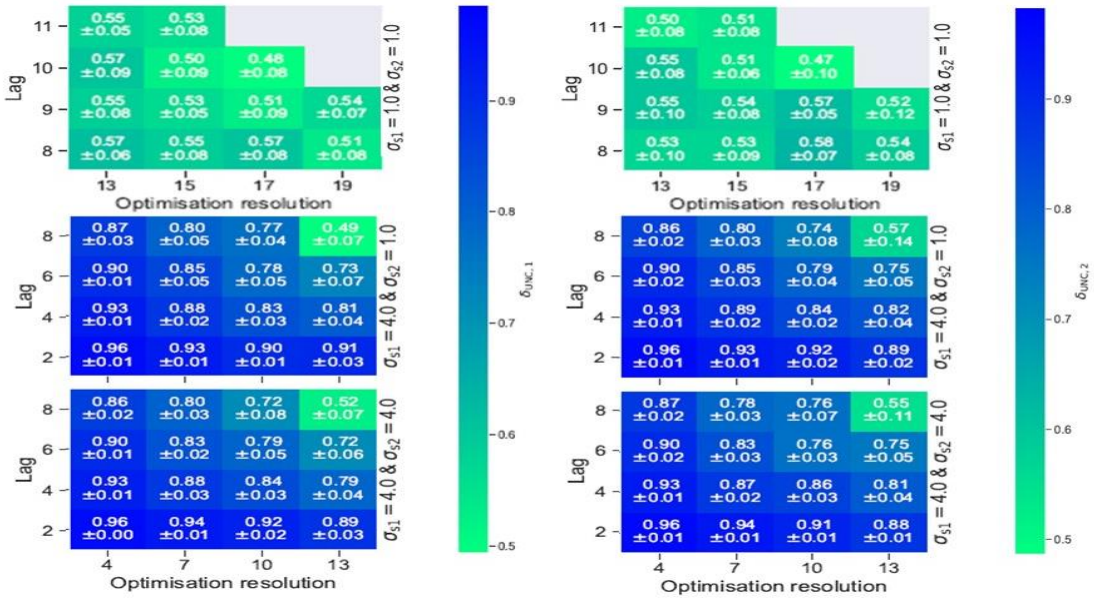

Figure 10. The ratio of posterior state variance to prior state variance (δ_{UNC}, color scale) for anthropogenic (left) and biospheric (right) flux components. Shown are different combinations

of the length of flux optimisation window (= optimisation resolution, days) and lag for two sets of state uncertainty parameters σ, 1 referring to anthropogenic and 2 to biospheric components.

3.2.1.2 The posterior flux uncertainty reductions

The posterior methane fluxes and their uncertainties were studied for the global TROPOMI satellite (InvWFMD and InvOPER) and surface inversions (InvSURF). For details see Tsuruta et al., (2023). In general, our results show smaller regional emissions in the TROPOMI inversions compared to the prior and surface inversion, although they are roughly within the range of the previous studies. The inversion results based on the two satellite datasets show many similarities in terms of spatial distribution and time series but also clear differences, especially in Canada, where CH4 emission maximum is later, when SRON's operational data are assimilated. The TROPOMI inversions show higher CH4 emissions from oil and gas production and coal mining from Russia and Kazakhstan. The location of hotspots in the TROPOMI inversions did not change compared to the prior.

The uncertainty reductions in the TROPOMI inversion are spatially more homogeneous, while the reductions are highest near the observational stations in InvSURF (Figure 11). This indicates that the good spatial coverage of the satellite data reduces the flux uncertainty on locations where the surface data are not available. Uncertainty reductions are often high in the regions where prior fluxes (and their uncertainties) are high and observations with small observational uncertainties are located. Such regions are found near anthropogenic sources in Europe, mid southern Canada and near biospheric sources in the HBL area in Canada and northern Europe (Figure 11). However, despite high biospheric emissions in Eurasian wetland regions, uncertainty reduction rates are not exceptionally high in all inversions. The uncertainty reductions in the Arctic ocean and some southern regions are high as those regions are optimized region-wise, i.e., there are more observations per optimization region as constraints.

The grid-wise uncertainty reduction rate is smaller in the TROPOMI inversions in general (Figure 11), although the regional posterior uncertainties are comparable to InvSURF in the NHL regions, and lower than InvSURF on a global level (Table 4). There could be a few explanations for this. First, temporal optimization resolution is different in InvSURF (seven days) and the TROPOMI inversions (three days). Since our assimilated data in the TROPOMI inversions are aggregated to to 1° x 1° x daily resolution, the number of observations may be twice larger in the surface inversion at the location where surface data are available (in situ data are also aggregated to daily values). In addition, the observational uncertainty for the satellite data is generally higher than those for the surface data. In general, when observational uncertainty is greater, there will be less influence on the optimization, leading to a smaller uncertainty reduction rate.

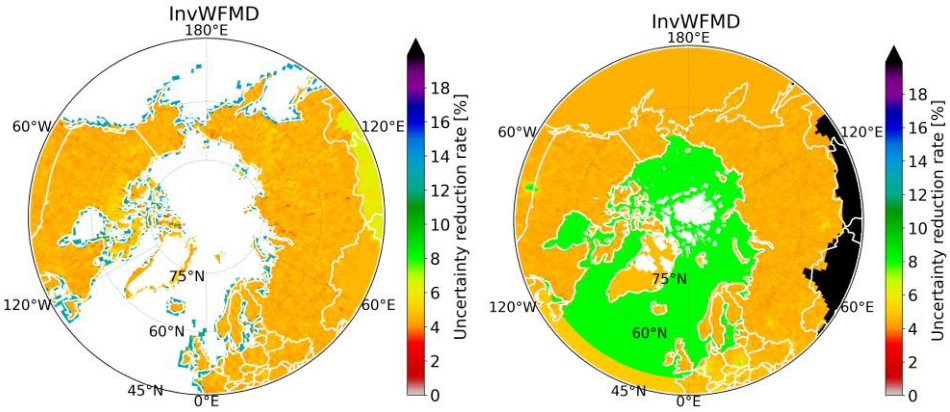

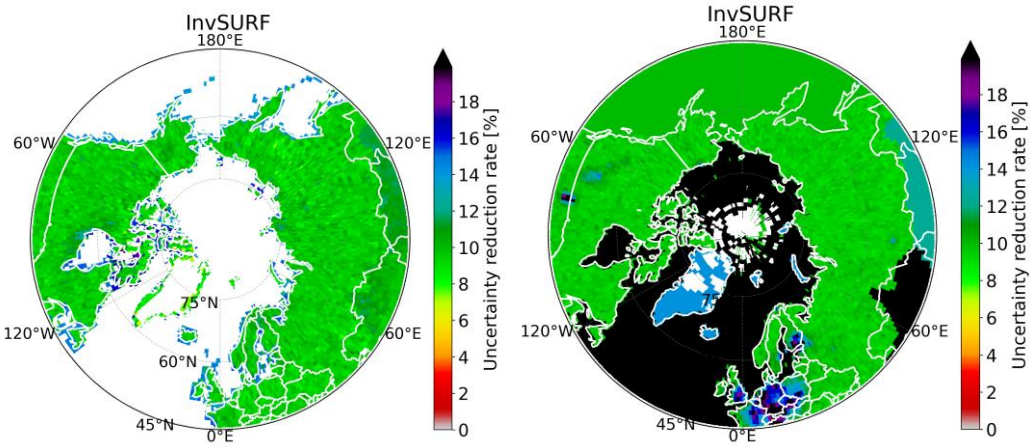

Figure 11. Annual mean uncertainty reduction rates above 45°N for 2018 estimated in InvWFMD (a,b) and InvSURF (c,d). The left columns (a,c) are for the biospheric fluxes and right columns (b,d) for the anthropogenic emissions.

Source	Simulation	Global	Above 45°N	Canada	Eurasia +Fennoscandia	Central Europe
Biospheric	Prior	118.72 ± 40.48	22.12 ± 0.90	7.62 ± 0.77	12.40 ± 0.99	2.10 ± 0.35
	InvWFMD	132.70 ± 35.74	20.09 ± 0.85	6.93 ± 0.73	11.17 ± 0.93	1.99 ± 0.34
	InvOPER	137.57 ± 37.31	19.93 ± 0.86	6.61 ± 0.74	11.30 ± 0.94	2.02 ± 0.34
	InvSURF	107.50 ± 36.89	23.65 ± 0.81	8.30 ± 0.65	13.23 ± 0.89	2.13 ± 0.32
Anthropogenic	Prior	373.69 ± 83.03	48.96 ± 2.84	7.45 ± 1.84	20.71 ± 3.17	20.80 ± 2.45
	InvWFMD	401.41 ± 50.65	41.75 ± 2.56	5.12 ± 1.67	20.39 ± 2.37	16.23 ± 2.27
	InvOPER	385.50 ± 57.92	42.36 ± 2.61	5.05 ± 1.69	19.92 ± 2.51	17.39 ± 2.31
	InvSURF	384.98 ± 69.76	51.44 ± 2.40	7.64 ± 1.40	20.20 ± 2.68	23.60 ± 1.68
Total	Prior	547.43 ± 92.55	84.56 ± 3.01	18.66 ± 2.05	39.14 ± 3.37	26.76 ± 2.47
	InvWFMD	589.14 ± 60.52	75.32 ± 2.73	15.64 ± 1.88	37.59 ± 2.62	22.09 ± 2.30
	InvOPER	578.09 ± 68.21	75.76 ± 2.78	15.24 ± 1.90	37.25 ± 2.74	23.27 ± 2.34
	InvSURF	547.50 ± 78.86	88.57 ± 2.56	19.53 ± 1.58	39.45 ± 2.86	29.59 ± 1.71

Table 4. Annual CH4 emissions and their uncertainty for 2018 (Tg CH4 / year). The uncertainties are calculated as standard deviation of the ensembles.

Secondly, we did not use so-called localization (Peters et al., 2005). Localization gives limits on how far in distance the observations can influence the fluxes. The grid-wise uncertainty reduction close to the observation location would be higher if the localization was used. When it is switched off, the uncertainty reduction is likely to be spread more equally in space, especially when observation uncertainties are correlated. This also indicates potentially high spatial correlation in the observation uncertainties, which is not properly taken into account in the inversions.

We assume observations to be uncorrelated in space and time in order to apply the ensemble square root filter (Peters et al., 2005). However, since the uncertainties in the satellite data could be highly correlated, the assumption may have not been valid. The TROPOMI retrievals errors showed the differences in the biases between snow and snow-free surface. The errors may be dependent region-wise over snow surface, but uncorrelated with snow-free surface (H, Lindqvist, personel communication). In addition, the observational uncertainty includes transport model uncertainty, which can be correlated based on, e.g., parameterization and input meteorological data.

The assumption of uncorrelated errors has been commonly used in atmospheric inverse models (e.g., Saunois et al., 2020). As discussed by Houweling et al. (2017) and references therein, accounting for the satellite data uncertainty is challenging. In this study, we assumed total observation uncertainty (transport model error + retrieval error) to be at a minimum of 20 ppb, and did not correct the spatiotemporal patterns of the errors before inversion. The uncertainty is within the range of those used in other satellite inversions using SCIAMACHY and GOSAT (e.g., Saunois et al., 2020). However, considering that the errors may be correlated, non-diagonal terms should have been compensated by higher standard deviations in the diagonal approximation. The TROPOMI data are assumed to have better precision than previous generation satellites, e.g., Lorente et al. (2021), but further examination is needed to quantify the appropriate uncertainty range to be used in the inversions.

3.2.1.3 Impact of prior error description

We examined the description of prior errors and the impact of the prior error on the posterior fluxes. Other than prior flux uncertainties, the inversion set-up was similar to InvSURF, assimilating surface observations. We applied the Carbon Tracker Europe – CH4 inversion model (Tsuruta et al., 2017) to study the effect of adjusting the prior biospheric flux uncertainties in optimization of the fluxes. We used Global Carbon Project model ensemble (Saunois et al., 2020) to define the range of prior biospheric flux uncertainties. As earlier, the magnitudes of the prior fluxes were obtained from LPX-Bern.

Previously, a fixed error (hereafter FIX) with proportion to prior fluxes (e.g., 80%) has been commonly used for biospheric fluxes (e.g., Tsuruta et al., 2017). Here we adjusted the error to be aligned with the range of GCP process model estimates (RANGE), and used this error to optimise biospheric emissions. The minimum uncertainty was set to 10% and the maximum to 500%. Uncertainty bounds were calculated for the optimisation regions, i.e. 1° x 1° in the high northern latitudes and regionally elsewhere. In addition, the seasonality of the emissions and their uncertainties were taken into account, and the uncertainty was defined on a monthly basis. RANGE generally had wider uncertainty bounds for the prior fluxes (Figure 12). Thus, the biospheric fluxes had more freedom for adjustment in the inversion. The spatial and temporal variability of the uncertainties was also higher than in FIX.

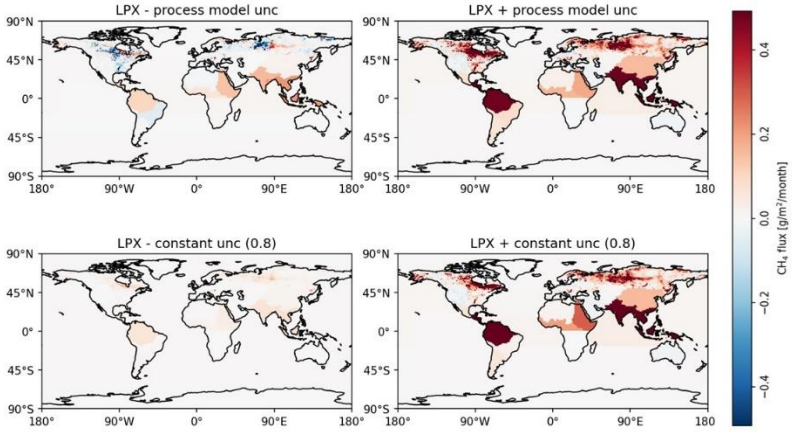

Figure 12. Annual mean prior biospheric flux uncertainty ranges using constant uncertainty factor of 0.8 (FIX, bottom figures), and GCP process model ensemble (RANGE, top figures), to define the lower flux error boundaries (left) and higher flux error boundaries (right).

The posterior biospheric fluxes using RANGE are shown in Figure 13. The fluxes are in average higher than using FIX, and the largest differences were found in the northern wetland regions in Canada and Russia, where prior fluxes were high and their uncertainty ranges changed the most. Large increases were also found in Southern America.

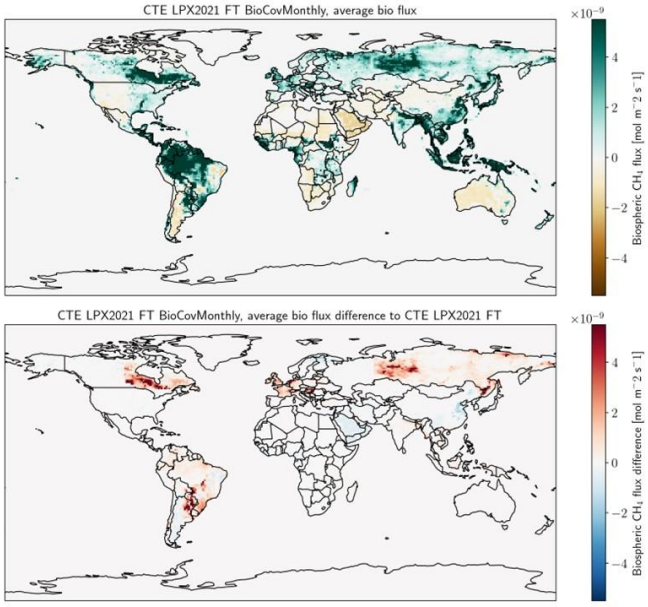

Figure 13. Posterior biospheric methane fluxes estimated by CTE-CH4 with RANGE presentation for prior flux errors, and the difference to FIX error presentation.

The global and high northern latitude flux time series (Figure 14) show higher fluxes in RANGE compared to FIX. Biospheric emissions are increased significantly in high northern latitudes (>10 Tg CH4 in 2016), and anthropogenic emissions are decreased. The high northern latitude total fluxes and their share in global emissions is also increased due to the increase in high northern latitude biospheric emissions. The seasonality of the global biospheric emissions is changed but mostly not due to high northern latitudes.

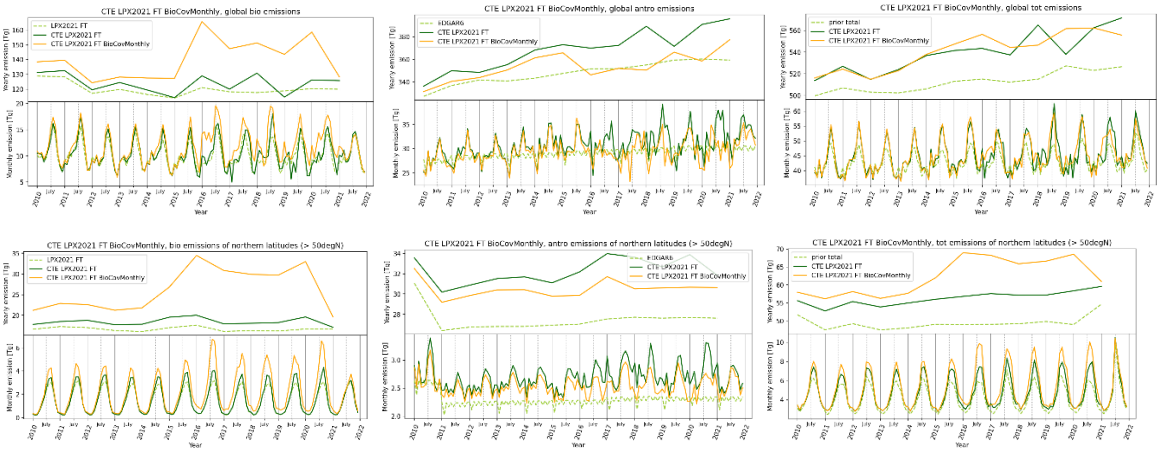

Figure 14. Annual mean and monthly biospheric (left), anthropogenic (middle) and total (right) methane fluxes. Global fluxes are shown in top figures and high northern latitude

fluxes above 50°N in bottom figures. Orange solid lines refer to posterior fluxes with RANGE and green to posterior fluxes with FIX.

The wider prior error boundaries in RANGE enabled the posterior increase of biospheric emissions, and some regional re-arrangement and changes in the seasonal cycle of emissions. Prior flux uncertainties are therefore an important component in optimization, that should be taken into account especially in regional and high resolution studies.

3.3 Conclusions

FMI studied the impact of the inversion set-up and assimilated data on the posterior methane flux uncertainty estimates of Carbon Tracker Europe – CH4 (CTE-CH4) atmospheric inversion model. We find that the regional monthly wetland emissions in the TROPOMI satellite inversions do not correlate with the anthropogenic emissions as strongly as those in the surface inversion. We find that the grid-wise uncertainty reduction rate is smaller in the TROPOMI inversions in general, but the uncertainty estimates in the TROPOMI inversions are more homogeneous in space, and the regional uncertainties are comparable to the surface inversion. This indicates the potential of the TROPOMI data to better separately estimate wetland and anthropogenic emissions, as well as constrain spatial distributions. The length of the assimilation window needs to be chosen depending on the set-up of the inversion and number of assimilated data on different temporal and spatial domains. Prior flux uncertainties have a significant impact on the optimised regional fluxes, on the share of the biospheric and anthropogenic emissions, and on the month-to-month changes in fluxes. The results emphasizes the importance of quantifying and taking into account the model uncertainties in regional levels in order to improve and derive more robust emission estimates.

4 Western Europe XCO2-CO2-14CO2 analytical inversion system

The following analysis is based on a high dimensional CO_2 analytical atmospheric inversion system covering Western Europe and assimilating XCO_2, surface CO_2 and/or $^{14}CO_2$ data. This system has been developed in the frame of the CO_2 Human Emissions project H2020 project (CHE, https://www.che-project.eu/), and used in the WP4 of this project, which evaluated the potential of measurements of tracers for fossil fuel CO_2 (FF CO_2) like radiocarbon, to support the separation between the biogenic and anthropogenic signals when assimilating CO_2 and XCO_2 data (see CHE D3.5, https://www.che-project.eu/node/242 and D4.4, https://www.che-project.eu/node/243).

Pseudo-data experiments (OSSEs) were conducted with this system to explore the complementarity between a CO2M-like spaceborne imager and surface CO_2 and $^{14}CO_2$ networks for the monitoring of the anthropogenic emissions of CO_2 at the regional to local scales. The analysis from CHE encompassed a general assessment of the respective potential of each type of observation component, or of their combinations. The analysis here complements this assessment by focusing on the added value of the surface $^{14}CO_2$ network depending on uncertainties in the natural fluxes of CO_2 and on the impact of nuclear emissions for the use of this tracer. This indirectly feeds the assessment of the need for including the natural fluxes and nuclear emissions in the inversion control vector when assimilating $^{14}CO_2$ data, even though the local variations of $^{14}CO_2$ are primarily driven by fossil fuel emissions. Potier et al. (2022) documents both the analysis from CHE and the following ones.

4.1 System Description

The details the inversion system are presented in the deliverables CHE D3.5 and D4.4 and in Potier et al. (2022). This section only provides a brief overview of the system. It relies on:

- A local to regional scale analytical inversion framework (Wang et al., 2018), which controls CO_2 anthropogenic emissions (fossil fuels, FF, and biofuels, BF) from large cities and industrial plants (point sources, PS) (Figure 15a), $^{14}CO_2$ nuclear emissions, regional budgets of more diffuse CO_2 emissions or of CO_2 natural fluxes (NEE) (Figure 15b) at hourly resolution, in addition to isotopic signatures (for the BF, and the soil heterotrophic respiration).
- A zoomed configuration of the regional atmospheric chemistry transport model CHIMERE (Menut et al, 2013) used to simulate CO_2 and $^{14}CO_2$ over most of Western Europe (Figures 15 and 16).
- Hourly to annual maps of all types of surface CO_2 and $^{14}CO_2$ fluxes, at high spatial resolution from CHE. They are used to distribute the local-to-regional-scale budgets of the fluxes into corresponding high resolution flux maps (Figure 16)
- Simulations of the locations and uncertainty of XCO_2 retrievals at 12:00 UTC and of hourly-CO_2 and 7-hour average $^{14}CO_2$ ground-based data between 10:00 and 17:00 UTC as a function of time, for different scenarios of the observing system (Figure 17, Table 5). For the XCO_2 data, we rely on the simulation of the CO2M sampling during one satellite overpass over the area of interest generated by the Institut für Umweltphysik, Bremen (IUP) in the frame of the ESA-PMIF project (Lespinas et al, 2020).

The system diagnoses the uncertainty in the values of the control variables from the inversion (the "posterior uncertainty") from the "prior uncertainty" assigned to the prior value of these variables that the inversion corrects to better fit the observations, from the observation sampling, and from the measurement and model errors (denoted together "observation

errors") based on the observation operator projecting the control space into the observation space (i.e., the sequence of the mapping of the fluxes, of the atmospheric transport model and of the sampling corresponding to the observations). Our experiences and analysis focus on this computation of the posterior uncertainty and on its comparisons to the prior uncertainties that are fixed through general assumptions on the accuracy of the inventories, of the models simulating NEE products etc.

Inversions are conducted over a 1-day window from 0:00 to 24:00 UTC, on July 1 2015, i.e., in summer, when the biogenic fluxes are relatively high.

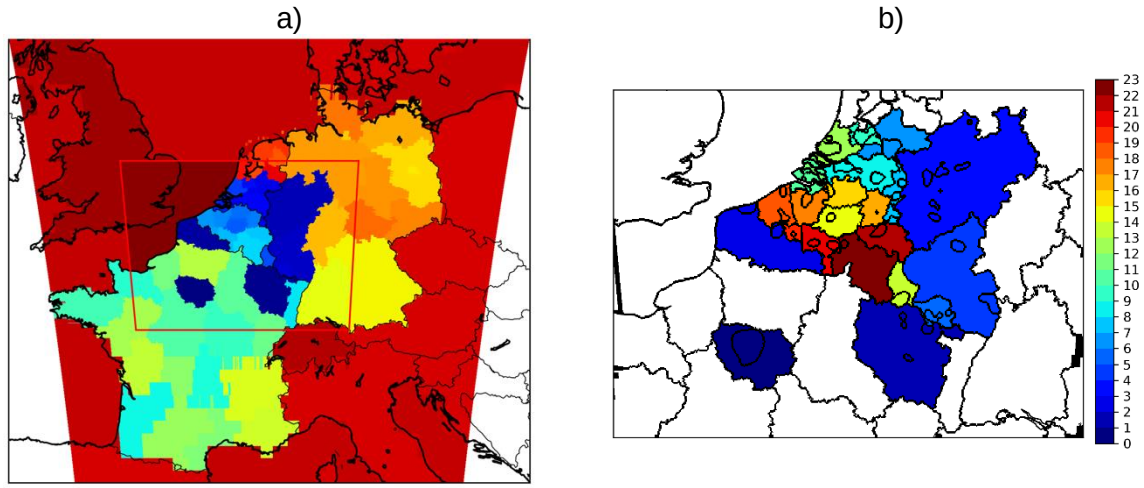

Figure 15: a) Administrative regions and coarser areas for which the CO_2 biogenic flux budgets and the anthropogenic emission budgets are controlled. The red line delimits the 2 km × 2 km resolution zoom of the CHIMERE transport model. b) Main area of interest in the 2 km × 2 km resolution zoom of the CHIMERE transport model, i.e. the 23 administrative regions where the CO_2 anthropogenic emissions from major urban areas (contours of the urban areas also represented here) and point source are controlled separately by the inversion.

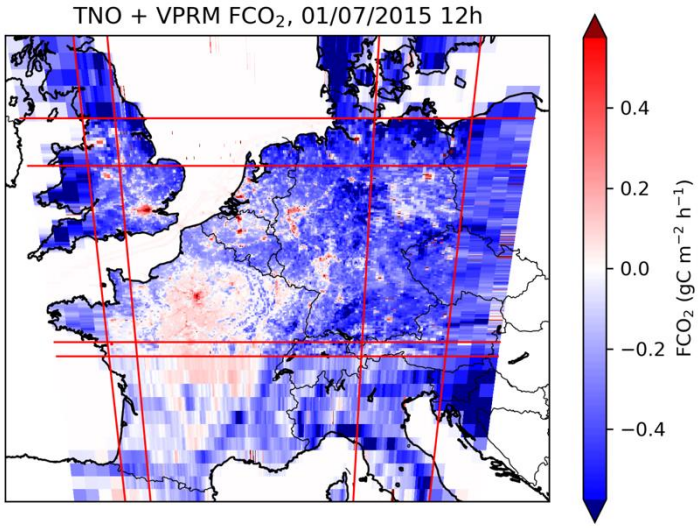

Figure 16: CO_2 flux map (based on values from the TNO inventory and VPRM simulations for 1 July 2015 at 12:00) over the atmospheric transport modelling grid. The red lines delimit the spatial resolution changes within the domain (from 2 km to 10 km and then 50 km from the middle to the edges of the domain)

a) **b)**

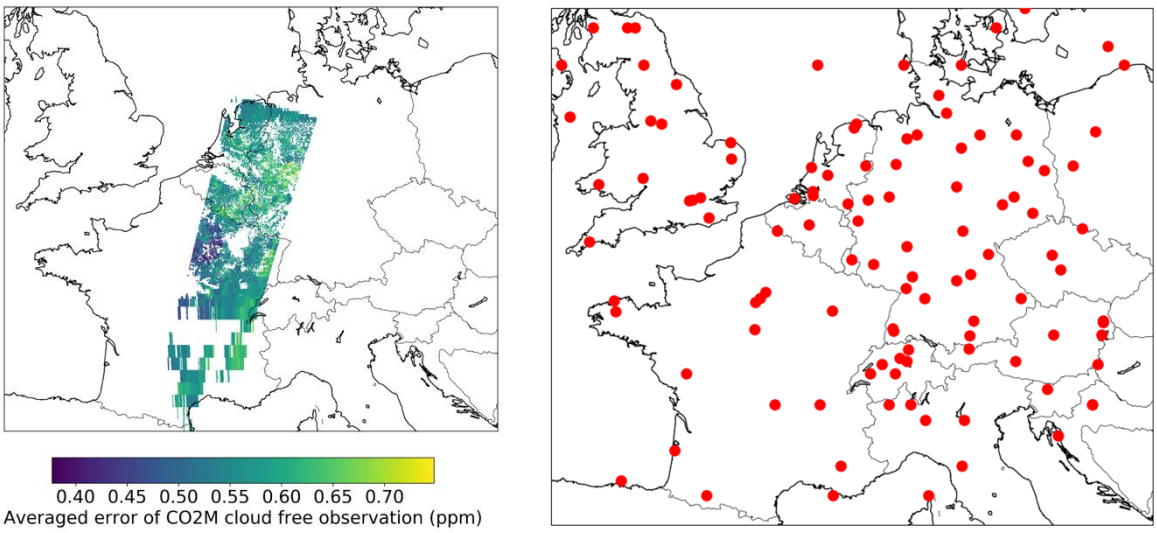

Figure 17: Observation system a) Simulation (from IUP / ESA-PMIF project) of the XCO_2 sampling and observation error standard deviation (in ppm) for a selected orbit of the spaceborne spectral imager set at 12:00UTC, b) Ground-based 7-hour average $^{14}CO_2$ and hourly CO_2 observation networks with 113 stations defined by Marshall et al. (2019), based on existing or potential measurement sites. The in situ data are used during the period 10:00-17:00.

Table 5: measurement, model, and total observation errors (1σ).

Error	Near-surface			Satellite		
	Meas	Model	Obs	Meas	Model	Obs
CO_2 (ppm)	0.05	1 to 5	1 to 5	0.38 to 0.75	1	1.07 to 1.11
$^{14}CO_2$ (ppm ‰)	200	405 to 2025	451 to 2034			

Table 6 provides labels for the different sets of experiments as a function of the sets of pseudo-observations that are assimilated, using or combining the satellite data, the surface CO_2 data and/or the surface $^{14}CO_2$ data (Figure 17).

Table 6: Labels for the different types of experiments

Inversion system observations	Name
Satellite XCO_2	INV-SAT
Surface CO_2	INV-CO2
Surface $^{14}CO_2$	INV-14C
Satellite XCO_2 + surface CO_2	INV-SAT-CO2
Satellite XCO_2 + surface $^{14}CO_2$	INV-SAT-14C
Satellite XCO_2 + surface CO_2 + surface $^{14}CO_2$	INV-SAT-CO2-14C

Here, the dependence of the added value of the $^{14}CO_2$ data to the uncertainties in the NEE or in the nuclear emissions is investigated by conducting sensitivity tests in which these uncertainties in the NEE or in the nuclear emissions are ignored, i.e., in practice, by excluding the corresponding components from the control vector of the inversion. For the sake of simplicity, we do not define specific labels for this and the text clarifies whenever diagnostics refer to the tests "ignoring/without NEE or nuclear emissions".

When analysing the results from the inversions and assessing the potential of the different types of observation networks, we focus on the standard deviation of the prior and posterior uncertainties in flux budgets, and on their relative difference (called uncertainty reduction or UR hereafter):

$$UR = 1 - \frac{\sigma_{post}}{\sigma_{prior}}$$

The definition of the prior uncertainties in the different control variables of the inversions is detailed in the deliverables from CHE (and in Potier et al. (2020)). It yields a ~30% uncertainty in the CO_2 fossil fuel emissions at scale of the day and of the individual administrative regions.

The surface data are assimilated between 10:00 and 17:00 only, and the satellite overpass occurs at 12:00 UTC, therefore the temporal footprint of the observational constraint for the correction of the prior estimate of the emissions depends on the observation network and does not cover the full day. This has been analysed in the deliverables from CHE and we do not address this topic here. Furthermore, the deliverables from CHE make a distinct assessment of the performances of the inversion of emissions at the scale of individual cities or point sources, which is not resumed here. Finally, this report does not repeat the conclusions of the deliverables from CHE regarding the decrease of uncertainties for the NEE itself and the BF emissions. The analysis for this new deliverable focuses on the results for FF CO_2 emissions at the scale of the day and of the regions. Emission budgets for a given region ("regional budgets") aggregate the emissions from the corresponding urban areas and point sources and the rest of the emissions within the region hereafter.

To evaluate the added value of ground-based networks, we define ΔUR^{Ref}_{Test} as the difference of UR for 24-h and regional budgets of FF CO_2 emissions between a test configuration and a reference configuration: $\Delta UR^{Ref}_{Test} = UR_{Test} - UR_{Ref}$. In these cases, the reference configurations are the ones when assimilating the data from the satellite track, either alone or with CO_2 data from the ground network (INV-SAT and INV-SAT-CO2 see Table 6).

4.2 Analyses

4.2.1 Constraints for the FF emission estimates from the different observation systems

This first subsection summarizes the type of analysis developed in the deliverables of CHE, with some updates of the results that are associated to various adjustments of the inversion configuration and experiments. It provides reference scores of UR for the assessment of the impact of uncertainties in the NEE and in the nuclear emissions.

When assimilating the data from the satellite track only (in INV-SAT inversion), the uncertainty reductions for the 24-hour regional budgets of FF emissions range from 0 to 18% in the main area of interest (Regions 1 to 23 in Figure 18).

Assimilating the data from the ground-based hourly CO_2 network only (in INV-CO2 inversion), reveals the limited role of the horizontal atmospheric transport near the surface to propagate URs from regions with several measurement stations to other regions (Figure 18). URs of more than 4%, (median at 12% and maximum at 13%), for 24-h budgets can be achieved in regions with 3 stations, like Île-de-France (Figure 18, Reg. 1, 12%), and North Rhine-Westphalia (Reg. 4, 13%) in the main area of interest, or in regions with more stations outside this area like southeast England (10%) and Baden-Württemberg (26%) which have 5 stations. However, the UR can also be much lower in regions with many stations, e.g. for Lower-

Saxony-and-Bremen which has 5 stations but a 4% UR. UR in regions with 1 or 2 stations range between 0% and 6%. The URs are generally below 1% for other regions. These URs reach lower or comparable values than in the INV-SAT experiment in the main area of interest. However, outside the main area of interest, Baden-Württemberg reaches a higher value than the largest one with the INV-SAT experiment (Rhineland-Palatinate, Reg. 5, 18%).

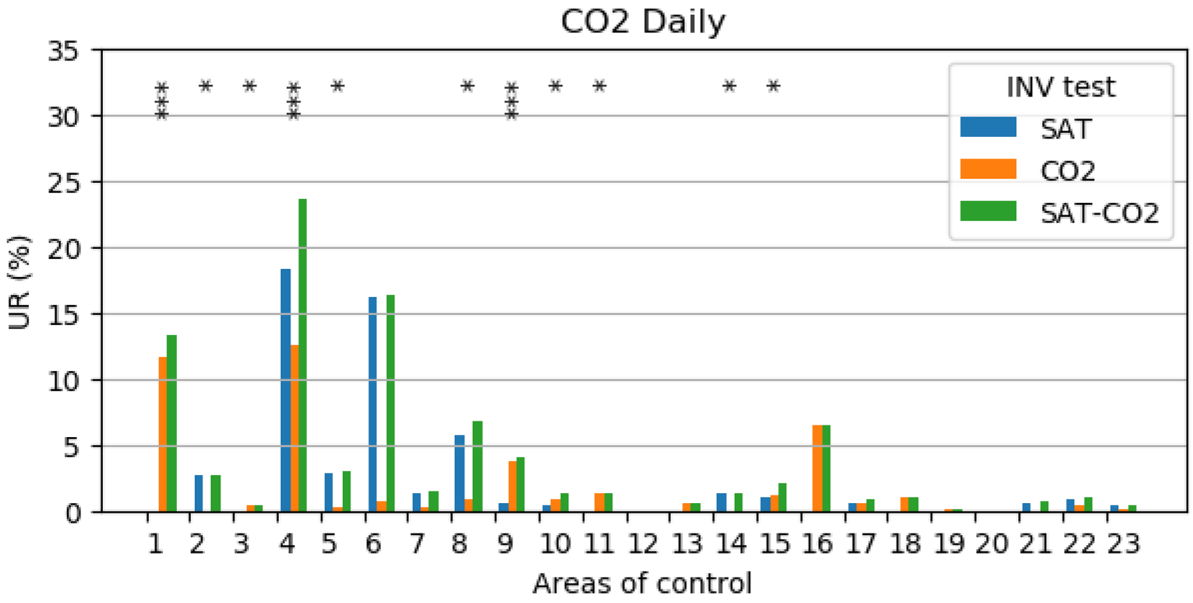

Figure 18: Uncertainty reduction in INV-SAT, INV-CO2, and INV-SAT-CO2 inversions for 24 h budgets of FF emissions of each controlled area in the main area of interest. The number of stars indicates the number of stations in each controlled area. The area numbers correspond to the ones in Figure 15b

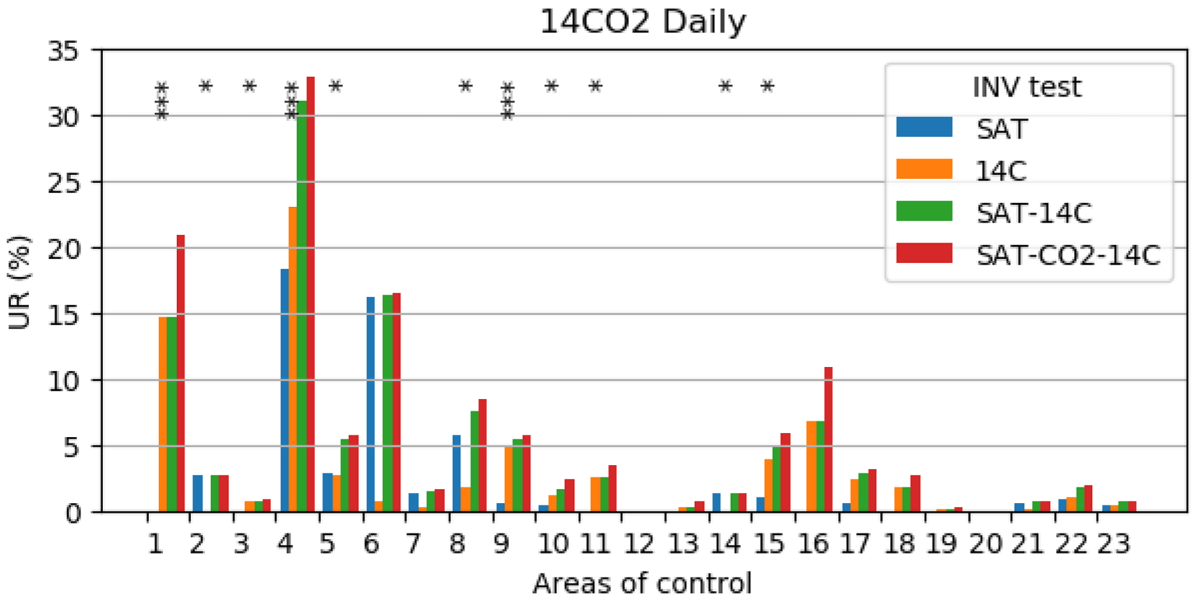

Figure 19: Uncertainty reduction in INV-SAT, INV-14C, INV-SAT-14C, and INV-SAT-CO2-14C inversions for 24 h budgets of FF emissions of each controlled area in the main area of interest. The number of stars indicates the number of stations in each controlled area. The area numbers correspond to the ones in Figure 15b

Only one region of the 2-km resolution model subdomain with 3 stations is located in the satellite FOV: North Rhine-Westphalia (Reg. 4). When comparing the URs for the 24-h regional budgets of FF emissions from INV-SAT-CO2 to that from INV-SAT and INV-CO2 (Figure 18) two significant changes can be seen. The first one is the increase of 5% of the UR for this region, i.e. less than the UR for this region in INV-CO2 (12%). The second one is the increase of UR for the regions outside the satellite FOV with more than 3 ground-based stations from nearly 0% to values that are nearly the same as in INV-CO2. The URs at 24-h scale in INV-SAT-CO2 are smaller than the addition of URs in INV-SAT and INV-CO2 experiment.

The spatial distribution of the regional URs for 24-h, when using surface 7-h-average $^{14}CO_2$ data alone is similar to that when using hourly-CO_2 surface data only (Figure 19). The URs on daily budgets are larger in INV-14C, i.e. when using the sampling of $^{14}CO_2$ representative of 7-h-averages of the mole fractions, than in INV-CO2, when using 7 hourly CO_2 data at each site. In most regions these differences remain relatively small except in Region 4, North Rhine Westphalia. The higher potential of $^{14}CO_2$ data (7-hour averages) than hourly CO_2 data to filter the signal from FF emissions, if both were measured at the same temporal resolution, is balanced by the finer temporal resolution of the hourly CO_2 continuous measurements. The hourly CO_2 data's finer temporal resolution helps capture the high frequency patterns of the signal from FF emissions. Section 3.2.2 further assess how much the uncertainties in the NEE lead to larger URs when using $^{14}CO_2$ data than when using hourly CO_2 data.

The fact that the URs for two combined networks is smaller than the sum of the URs for the individual networks that was shown when comparing INV-SAT, INV-CO2 and INV-SAT-CO2, also applies when adding the surface network i.e. when comparing e.g. INV-SAT-14C to INV-SAT and INV-14C or INV-SAT-CO2-14C to INV-SAT-CO2 and INV-14C. The combination of 7-h-average $^{14}CO_2$ data with other types of data does not lead to further synergies of the advantages for each network: the spatial extent of the satellite observation, the temporal coverage of the ground-based networks, the temporal resolution of the hourly-CO_2 surface network, and the higher sensitivity to FF emissions of the 7-h-average 14CO_2 network. In North Rhine-Westphalia, where the configuration is favourable, with 3 stations in the satellite FOV, the UR for the daily budget increases from 18% with INV-SAT to 33% with INV-SAT-CO2-14C (Figure 19, Reg. 4). This configuration leads to 6.6% posterior uncertainty. In Ile-de-France (Reg. 1) outside the satellite FOV and with 3 stations, the UR reaches 21% in INV-SAT-CO2-14C, reaching 18% posterior uncertainty. In Saarland (Reg. 6), in the satellite FOV and without stations, the UR remains similar in INV-SAT-CO2-14C as in INV-SAT, 17%, corresponding to 15% posterior uncertainty.

4.2.2 Impact of the uncertainty in the Net Ecosystem Exchange

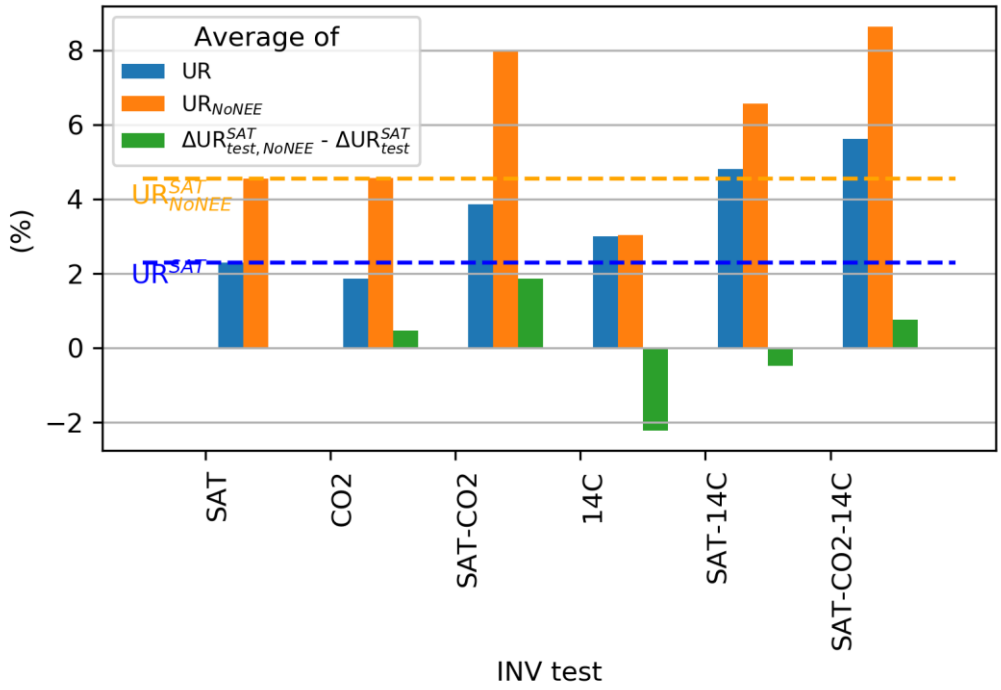

Figure 20: Average on the main area of interest of the UR on 24 h FF regional budgets in a set of inversion configurations, with (blue) and without (orange) NEE and average of the difference between ΔUR^{SAT}_{Test} with and without NEE (green). Negative values highlight an increase in the additional observation network potential when NEE is taken into account. Positive values highlight a decrease in the additional observation network potential when NEE is taken into account. High absolute values highlight strong NEE impact.

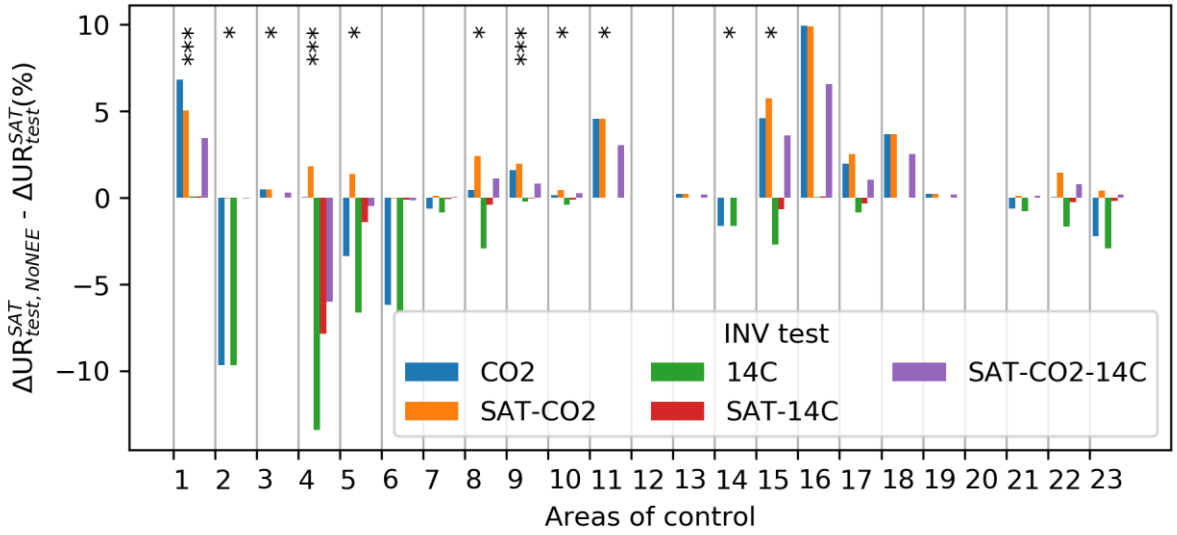

Figure 21: Impact of the NEE on the ground network capability at the top of the satellite observations for each area of control in the main area of interest: differences between ΔUR^{SAT}_{Test} on 24 h FF regional budgets, with and without NEE. Negative values highlight an increase in the additional observation network potential when NEE is taken into account. Positive values highlight a decrease in the additional observation network potential when NEE is taken into account. High absolute values highlight strong NEE impact. The number of stars indicates the number of stations in each controlled area. The area numbers correspond to the ones in Figure 15b

The INV-SAT experiment ignoring the NEE shows significantly larger URs for the FF regional 24-h budgets (Figure 20). This increase of the URs yields posterior uncertainties in 24-h regional budgets which can reach values as low as 6.7% in the satellite FOV (not shown). The surface network has many stations mostly sensitive to the NEE signal, therefore it is expected to support the distinction between NEE and FF emissions in the inversion, even when the stations measure CO2 only. In inversion INV-CO2, the UR for FF emissions is higher when ignoring the NEE, reaching a range between 18 % and 46 % for 24 h budgets in the regions with more than three stations. However, the comparison between results from INV-SAT-CO2 and INV-SAT when ignoring these fluxes hardly demonstrates a potential of the surface CO2 network to reduce the problem of attribution between FF emissions and the NEE (Figure 20). Figure 20 shows $\Delta UR^{SAT}_{SAT-CO2,NoNEE}$ larger than $\Delta UR^{SAT}_{SAT-CO2}$ on average; i.e. adding the CO2 network when ignoring the NEE yields a larger increase in the UR than when accounting for NEE. This is linked to the smaller UR associated with CO2 data when accounting for NEE. There is a lack of indirect feedback on the UR for FF emissions from the lowering of uncertainties in NEE when complementing the satellite data with CO2 data.

Concerning the impact of NEE, in INV-14C, the URs for FF emissions in the regions with more than three stations are higher when ignoring the NEE, reaching a range between 15 % and 33 % for 24 h budgets. The comparison of the experiments INV-14C with and without NEE shows a much smaller impact of NEE on the URs for FF emissions than in experiments INV-CO2 or INV-SAT, which is directly linked to the much smaller sensitivity of 14CO2 data to NEE than CO2 data. An interesting consequence is that, on average, ΔUR^{SAT}_{14C}, $\Delta UR^{SAT}_{SAT-14C}$ (Figure 20) or $\Delta UR^{SAT-CO2}_{SAT-CO2-14C}$ (not shown) is slightly larger when accounting for the NEE than when ignoring it.

The potential of the 14CO2 network to complement the satellite observation is higher when NEE is accounted for, while the result for the surface CO2 network is the opposite. This increase in the impact of the 14CO2 network when accounting for NEE is however relatively small, reaching its maximum in the region of North Rhine-Westphalia, which has three stations, and where the posterior uncertainty decrease for the 24 h regional budgets of FF emissions from INV-SAT to INV-SAT-14C is 15 %.

4.2.3 Impact of the 14CO2 Nuclear Emissions

The impact of nuclear emissions in the inversions assimilating 14CO2 data is analysed by conducting experiments where these emissions are ignored. The comparison of INV-14C experiments with and without nuclear emissions shows an increase of the URs, in the range of 0-1.7 percentage points (Figure 22), when these nuclear emissions are ignored. In the main area of interest, the most impacted areas are the Zeeland, Brabant/Bruxelles, Anvers and Flanders, which are regions where the stations are close to nuclear sites (Figure 22). Outside the main area of interest, similar to what is seen in this area of interest, the impact is generally low but it can reach up to 9% points difference for Baden-Wurttemberg , - (Figure 22).

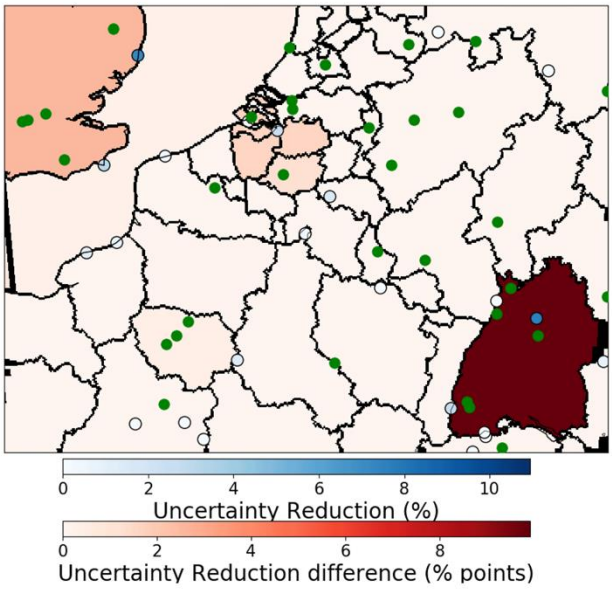

Figure 22: Maps of the 2 km resolution area with the differences between uncertainty reductions on 24 h FF budgets with and without nuclear emissions (shades of red) in INV-14C inversions and uncertainty reductions on F14C emission budgets from nuclear sites (dots, blue palette). Green dots indicate the ground stations.

4.3 Conclusions from the experiments with the Western Europe XCO2-CO2-14CO2 analytical inversion system

The new analysis in CoCO2 with the Western Europe XCO2-CO2-14CO2 analytical inversion system from CHE confirms the natural assumption that the added value of 14CO2 surface networks is emphasized when the uncertainties in the NEE are large. However, accounting for the uncertainties in the NEE, as well as accounting for the uncertainties in the nuclear emissions, impact significantly the results from inversions assimilating 14CO2 data only. Together with the conclusions from the experiments conducted in CHE, this supports:

- the deployment of very dense CO2-14CO2 surface networks to support the satellite observation for regional to local scale inversions of CO2 emissions

- the use of extended control vectors when co-assimilating CO2 and 14CO2 observations to derive FF CO2 emissions, accounting, in particular, for the regional scale uncertainties in NEE and for uncertainties in the radiocarbon emissions from individual nuclear sites. Accounting for the uncertainties in the radiocarbon emissions is, on average, much less important than accounting for the uncertainties in the NEE, but it can have a significant impact for specific regions.

5 LOTOS-EUROS

5.1 System Description

The LOTOS-EUROS regional emission inversion system is based on a 4D-var approach. In the CoCO2 project, the model domain covers Europe on coarse resolution (10-25 km). The inversion system specifies uncertainties in emissions in terms of gridded fields of adjustment factors; the 4D-var inversion then searches for an optimal set of emission adjustment factors that give the best match with observations, taking into account the observation representation error of the model.

The parameterization of the *a priori* emission uncertainty is one of the main inputs to the inversion system. It defines the freedom that the inversion system has to change the emissions both in space and in time. Traditionally, the emission uncertainty is parameterized by a set of standard deviation and spatial and temporal correlation lengths. These parameters should be tuned such that the range of possible emissions could explain for a large part the difference between the simulations and the observations. If the possible range of emissions is too small, the inversion system will not be able to find optimal emissions that give a good match with the observations, or it will provide “optimal” emissions that are outside the assumed uncertainty range. If on the other hand the allowed range of emissions is too large, the inversion system will easily find an optimal emission set, but one might wonder how realistic the assumed uncertainty is. In any case it is also important to consider that uncertain emissions are not the only cause of a difference between simulations and observations, as also for example boundary conditions and model transport errors contribute to this.

For preparation of an inversion it is therefore important to evaluate the *a priori* emission uncertainty in detail. Within the CoCO2 project, TNO has prepared an uncertainty parameterization together with its CO_2 emission inventory. In the study described here, this uncertainty is evaluated to see what the impact is on model simulations. Simulations with LOTOS-EUROS are performed to investigate the impact of the allowed variability in the emissions on simulated mixing ratios. This will provide a first insight in whether the specified uncertainty is sufficient to explain the difference between simulations and observations, or that other sources of uncertainty are needed to explain this.

5.2 Analyses

5.2.1 Emission uncertainty parameterization

An uncertainty parameterization is available for the TNO-GHGco-v4 emission inventory for 2018, as used throughout this project. The inventory provides anthropogenic emissions of Green House Gasses and co-emitted species at a resolution of 0.10^ox0.05^o (about 5x5 km and European latitudes). For CO_2, the inventory distinguishes emissions due to fossil fuels and bio fuels. Figure 23 provides an example of the fossil-fuel related CO_2 emissions provided in this inventory.

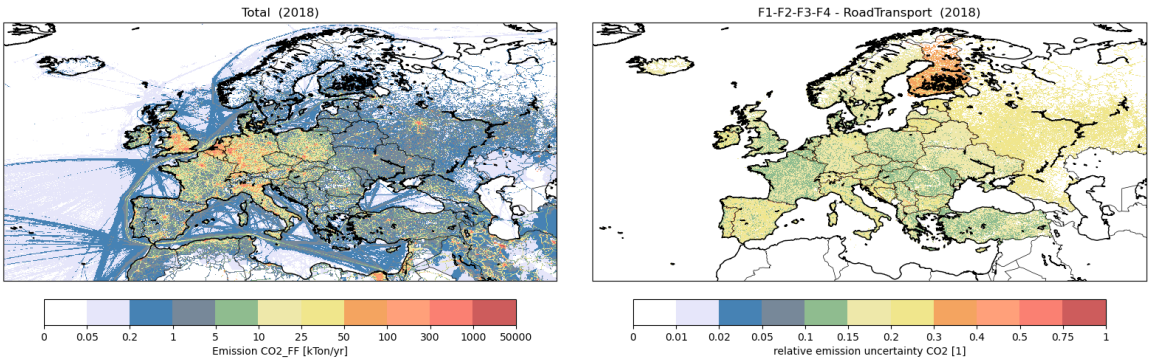

Figure 23: Left: Fossil-fuel related CO_2 emission in the TNO-GHGco-v4 inventory. Right: standard deviation of relative uncertainty per grid cell for CO_2 RoadTransport emissions.

For the CoCO2 project, a parameterization of selected uncertainties for the fossil fuel related emissions has been created too. The uncertainties are described in detail in Super *et al.*(2023, *submitted*); here we summarize what is available in the parameterization and how it can be used to create an ensemble of realistic emissions.

The uncertainty parameterization used here was tagged v2.0. To create uncertain CO_2 emissions as model input, the following content is used:

1. A standard deviation for the relative uncertainty of each individual CO_2 emission in the inventory. The inventory consists of a list of emissions that represent an area emission in a grid cell or a point source emission, for a specific source sector and country, and for each of these a number is available. An example of the standard deviations for the source category RoadTransport is provided in the right panel of Figure 23. The map shows clearly the country borders, as the gridded standard deviations have been determined based on country reports of emissions and associated uncertainties.
2. A spatial correlation length scale L in km, for each of the source categories. This defines the correlation $r_{i,j}$ between the uncertainty of an emission in a grid cell i and the uncertainty of an emission in another grid cell j that are at distance $d_{i,j}$ in km from each other; the correlation is defined following an exponential profile:

$$r_{i,j} = e^{-d_{i,j}/L}$$

Table 7 shows the length scales per source category. Only for categories *Other stationary combustion* (which includes for example domestic heating), *Road transport*, and *Shipping*, a length scale is defined.

The uncertainty in a country total is defined by the combination of the standard deviation field and the spatial correlation. Ultimately, the uncertainty in the country total computed in this way should match with the uncertainty reported for each country, but that is not yet the case in the current uncertainty product. For new releases of the product it is planned that the standard deviation fields are scaled per country to ensure that the totals do actually match, but for the moment, the reported country uncertainties are simply ignored and we assume that the standard deviation field defines the uncertainty together with the length scale. For most categories a zero length scale is assumed, since these are either dominated by large point sources (such as categories A (*Public Power Generation*) and B (*Industry*)), or because no information on length scales could be derived. The emissions from these categories in two grid cells could therefore differ from their *a priori* value in opposite direction, even if these cells are close to each other. The gridded standard deviations for these categories is high (usually 100%), but since no spatial correlation is assumed, the uncertainty in a country total is smaller as both higher and lower emissions than the *a priori* values occur.

Table 7 – Emission source categories and associated correlation length scale

GNFR	Source category	L [km]
A	Public Power Generation	0
B	Industry	0
C	Other stationary combustion	26
D	Fugitives	0
E	Solvents	0
F	Road transport	23
G	Shipping	100
H	Aviation	0
I	Offroad transport	0
J	Waste treatment	0
K	Agricultural livestock	0
L	Agricultural other	0

5.2.2 Emission ensemble

An ensemble of *N*=20 possible emission files has been drawn out of the uncertainty definition. The following steps were taken:

1. For each of the 3 correlation lengths *L* that are used, an eigenvalue factorization of a spatial correlation matrix C_L defined on the emission grid was created: $C_L = Q_L \Lambda_L Q_L^T$The elements of C_L are set to spatial correlation between two source cells given their distance and the correlation length scale following the exponential decay. One side of the correlation matrix C_L has a size to the number of grid cells in the emission domain, which is here 756,000 in total. The full matrix C_L would be too large to be stored, and therefore it is only defined as an operator that computes non-zero elements. The eigenvalues in the diagonal matrix Λ_L and vectors in Q_L are then computed using Arnoldi iterations. For larger length scales the eigenvalue spectrum drops quickly to zero, and therefore it is sufficient to only compute the largest eigenvalues and corresponding eigen vectors. However, the factorization is computationally still very demanding, and takes multiple days to be finished.
2. An ensemble of *N* random samples is drawn from the distribution defined by the factorized correlation matrix using:

$$x_{L,i} = Q_L \Lambda_L^{1/2} w_{L,i}, i = 1, .., N$$

$w_{L,i}$ is a random vector with a size equal to the number of eigenvalues in Λ_L drawn out of the normal distribution. Each vector $x_{L,i}$ represents a possible field of emission perturbations out of a distribution with spatial correlation *L*.

3. An ensemble of *N* realistic emission inventories is created as a perturbation of the *a priori* emissions. For a source category *s* that is spatially correlated with length scale *L* the perturbed emissions are:

$E_{s,i} = E_{a,s}(1 + \sigma_s x_{L,i})E_{a,s}$ represents the *a priori* inventory for category *s* and σ_s the corresponding standard deviation field. For a spatially uncorrelated category the perturbed emissions are:

$E_{s,i} = E_{a,s}(1 + \sigma_s v_{s,i})v_{s,i}$ is a random field with the size of the source cells drawn from the normal distribution. The random numbers might cause negative emissions which are then reset to zero.

The impact of the uncertain emissions on simulated CO_2 mixing ratios has been evaluated with the LOTOS-EUROS model. For each of the *N* emission perturbations a simulation has been performed over 2018, each using a different perturbed emission fields as input, but using the same temporal distribution within the year, and the same (climatological) boundary conditions, biogenic emissions, and biogenic uptake.

Figure 24 shows maps of the total CO_2 emission over 2018 on the model resolution (left panel), and the standard deviation in the ensemble of emissions (right panel). The emissions are especially strong at locations of power plants, which are often located in more remote areas and not surrounded by other sources. Also, the uncertainty is relatively strong at these locations. Larger areas with strong emissions are present in England, Netherlands, German Ruhr area, and Italian Po-valley. These areas are however not similarly visible in the standard deviations, since for example the standard deviations for road traffic emissions are rather small due to the assumed spatial correlations. At rural locations the standard deviation seems often higher than the (rather low) emission values; investigation showed that this is caused by the rather high standard deviations of 100% assumed for some source sectors. Another remarkable feature is that there is no uncertainty in the shipping emissions over the Atlantic Ocean and Mediterranean, which is a result of the standard deviations actually being zero for the international shipping in the uncertainty inventory.

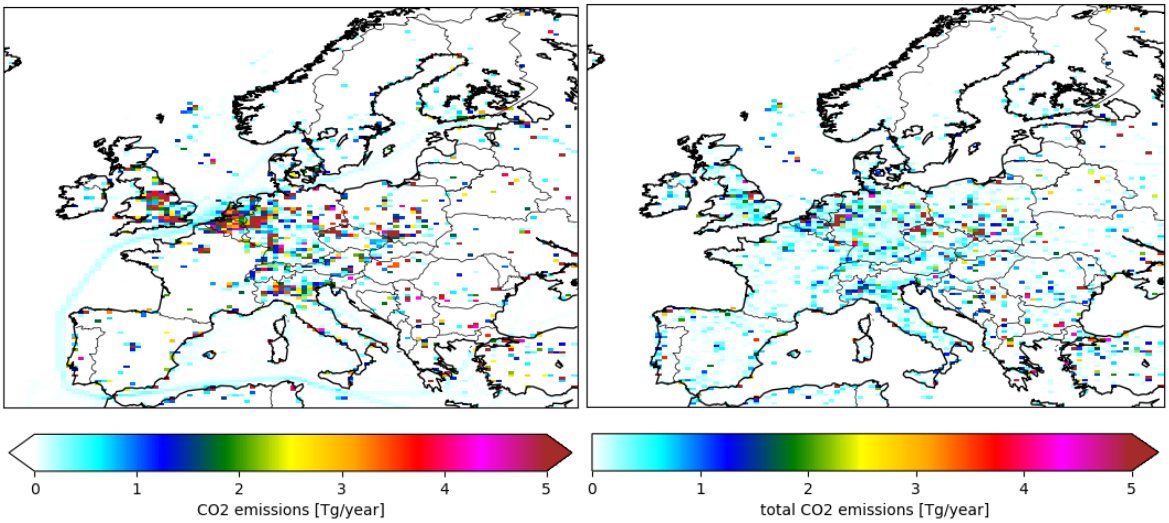

Figure 24 – Map of total CO_2 emission in 2018 from CoCO2 inventory (left), and standard deviation in the derived ensemble of perturbed emissions (right).

5.2.3 Simulated mixing ratios

The simulated CO_2 mixing ratios in the ensemble provide a first insight on the impact of the uncertainty defined for the fossil-fuel related emissions.

As example, Figure 25 shows the ensemble mean (left) and standard deviation (right) of monthly averaged surface mixing ratios of CO_2 at 15:00 for June-August 2018. At this time of the day, the atmosphere is assumed to be well mixed and mixing ratios are less sensitive to local sources. Highest mixing ratios are seen over land, with even higher mixing ratios over urbanized locations, such as the German Ruhr area and northern Italy. These urbanized locations also have the highest standard deviations (right panel) as the ensemble is driven by uncertainty in anthropogenic emissions. In general, the uncertainty in mixing ratios decreases quickly with distance from the source locations, since the differences in mixing ratios are for example damped by the biogenic uptake or do not reach the surface at all. This suggests that the specified uncertainties in the fossil-fuel related emissions are only visible at measurement locations that are close to, or surrounded by, these emissions. An inversion system that aims at reducing these emissions should therefore analyse the observations from such locations and could not rely only on remote sites.

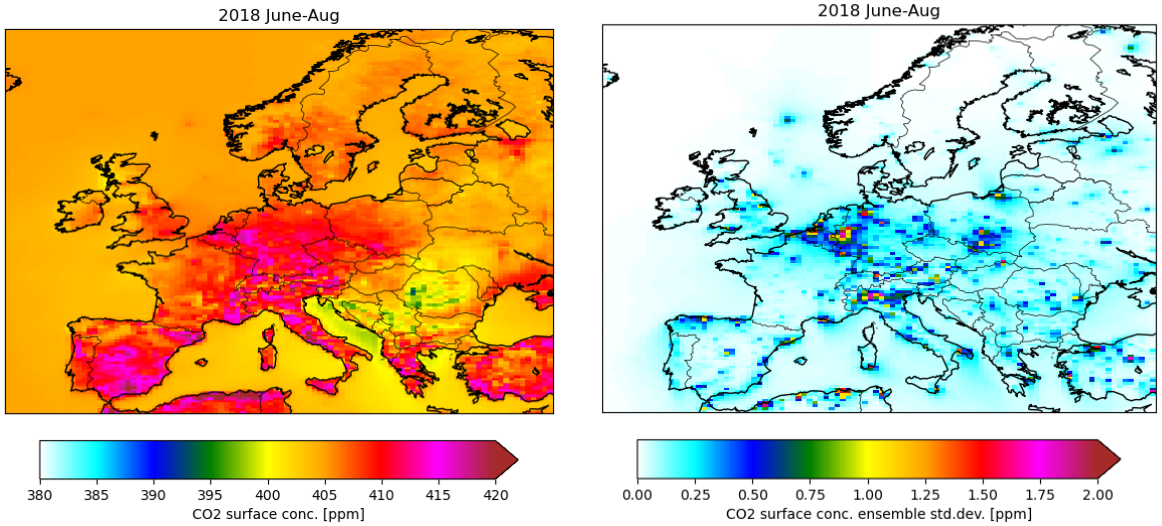

Figure 25 – Ensemble mean (left) and ensemble standard deviation (right) of monthly averaged CO_2 surface mixing ratios at 15:00 for May 2018.

5.2.4 Concentrations at observation sites

Observations of CO_2 for 2018 have been collected from the ICOS portal. For each of the observation locations, timeseries of simulated mixing ratios were extracted from the ensemble. The difference between the observations and a model simulation is partly due to uncertainty in fossil fuel emissions that defines the ensemble; assimilation of these observations might reduce this uncertainty and lead to better emission estimates.

To see which of the observation sites are sensitive to the uncertainty in the fossil fuel emissions, Figure 26 shows the maximum standard deviation in the ensemble at 15:00 within the period June-August. For stations within the boundary layer, the afternoon samples are usually those that are used in an assimilation as the atmosphere is then well mixed, and observations are not strongly influenced by nearby sources. The result shows that the maximum standard deviations are found for stations Lutjewad in the north of the Netherlands, Lindenberg in the east of Germany, and the Observatoire Pérenne de l'Environment in the north of France. These sites are in the selected season influenced by fossil fuel emissions

from the urbanized areas of The Netherlands and Germany, and probably also emissions from power plants in the east of Germany.

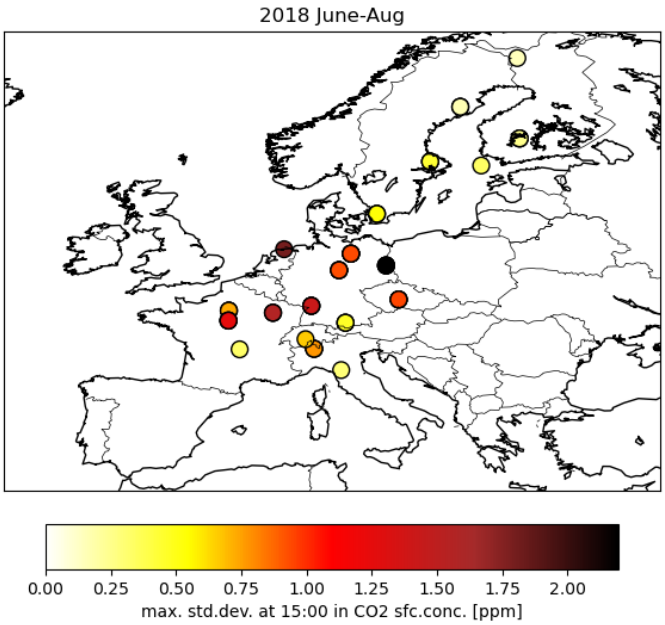

Figure 26 – Maximum std.dev. over Jun-August in simulation ensemble

As illustration, a time series of the CO_2 mixing ratio's in Lindenberg at 15:00 is shown in Figure 27. The maximum ensemble standard deviation that was shown in Figure 26 occurs halfway August. The spread in the ensemble is then able to explain a large part of the difference between the model and observations. That is however not the case for most other days, where the spread in the ensemble is usually small. The model is in general able to simulate the mixing ratio levels at the site, except for the first weeks of June, where the model strongly under-estimates the observations. The large discrepancy during this period cannot be explained from uncertainty in emissions only, and is likely to be at least partly due to uncertain background mixing ratios from the boundaries.

Investigation of the time series in other stations and other seasons lead to similar results. For selected sites and selected periods, the spread in the ensemble is sufficiently large to explain part of the difference between simulations and observations, but more often it is rather small, and other uncertainties are needed to explain the difference between observations and simulations.

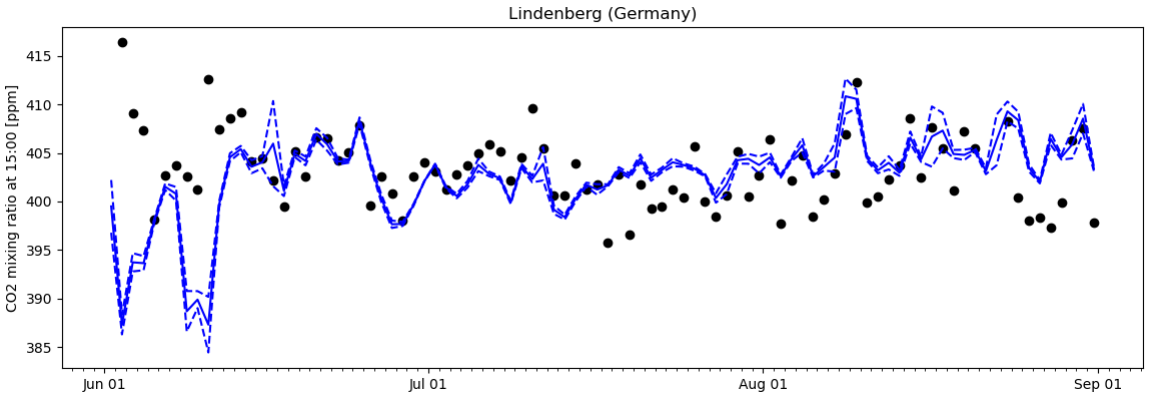

Figure 27 – Time series of CO_2 mixing ratio's at 15:00 in ICOS site Lindenberg (Germany); black dots are observations, blue solid line ensemble mean mixing ratio's, with dashed lines the 2-sigma ensemble spread.

5.3 Conclusions

Specification of uncertainties in a simulation model and its input is an essential part of an inversion system. In this study, the uncertainty parameterization v2.0 for fossil fuel related emissions that is available for the TNO/GHGco v4.0 European emission inventory has been evaluated for its use in an inversion system.

The uncertainty parameterization provides (among others) for each of the major emission source categories a standard deviation value for each point or area source and a horizontal correlation length scale. Together these could be used to draw random samples of realistic emission inventories. From the process of generating such samples the following recommendations are made:

- The common method of generating horizontally correlated samples uses an eigen value decomposition of a spatial correlation matrix. For the high resolutions on which current emission inventories are defined this becomes a computationally demanding task. Alternative methods should be developed for this. Such alternative methods would also benefit variational inversion systems, which use the eigenvalue decomposition to efficiently evaluate the prior term in the cost function and its gradient.
- For source categories without assumed spatial correlations (mainly dominated by point sources), the assumed standard deviation is large (100%), which lead to random samples that could be negative. The standard deviations should however be interpreted as defining a log-normal distribution, which would avoid occurrence of negative values. If this interpretation is used consequently, one should interpret the ensemble statistics in terms of median and geometric standard deviation.
- The uncertainty parameterization shows some unexpected features, for example a zero uncertainty for international ship tracks. This is mainly related to the fact that in the current release the standard deviation field is not matched with the country total uncertainty (taking into account the length scale). This will be taken into account in future releases, however.

An ensemble of realistic emission inventories has been drawn from the uncertainty parameterization and was used as input for the LOTOS-EUROS simulation model. The spread in the simulated CO_2 mixing ratios is largest over urbanized area with high emissions from, for example, road transport, and at locations near power plants. At observation sites from the ICOS network this spread is hardly visible however, as these are often located at more remote locations. Only occasionally the specified uncertainty in fossil fuel emissions is able to explain the difference between simulations and observations at some of the ICOS sites. A preliminary conclusion is that the uncertainties in emissions that are usually assumed in inversion systems

are higher than what is specified in the current emission uncertainty parameterization. Further research is therefore needed to make best use of the new uncertainty information in an inversion.

6 Conclusion

With the work performed here in Task 5.5 we have explored the impact of specific but reasonable choices in the design/set-up of the modelling systems on the posterior uncertainty representation of the CO_2/CH_4 fluxes. This has been done using various inverse modelling / data assimilation approaches to reflect the range of modelling systems but also because some of the design options could only be assessed in specific systems. The DA systems applied here cover scales from global (CCFFDAS), European (CTE-CH4, LOTOS-EUROS) down to regional/local (LSCE's Western Europe analytical inversion system, local CCFFDAS set up around Berlin).

The four modelling groups (iLab/ULUND, LSCE, FMI and TNO) have gathered a large amount of results about the contribution of the chosen in situ network, inclusion of $^{14}CO_2$, length of the assimilation window, prior uncertainty description, set-up of the control vector, and approximation of posterior uncertainty quantification on the posterior uncertainties.

With the CCFFDAS several design options have been analysed at either global scale or local scale. For example, each additional satellite in the CO2M constellation achieves a further reduction in posterior uncertainty at country scale in the sectoral fossil fuel emissions. In addition, the performance of in situ networks is generally weaker compared to observations from CO2M. CO2M provides two more observational data streams: atmospheric aerosol information from a Multi-Angular Polarimeter (MAP) and atmospheric NO_2 concentrations. Better information on the atmospheric aerosol load through the MAP generally improves the impact of the CO2M, but over the study region around Berlin the impact of the MAP is particularly high in winter. Adding NO_2 observations has a strong impact on the emission quantification of larger power plants as well as the emissions from the entire city of Berlin.

The analysis with the Western Europe XCO2-CO2-14CO2 analytical inversion system has demonstrated the added value of $^{14}CO_2$ surface observations in fossil fuel emissions estimations especially in cases when the uncertainties in the NEE are large. However, accounting for the uncertainties in the NEE as well as accounting for the uncertainties in the nuclear $^{14}CO_2$ emissions impact significantly inversion results. Accounting for the uncertainties in the radiocarbon emissions is, on average, much less important than accounting for the uncertainties in the NEE, but it can have a significant impact for specific regions.

For assessing the impact of inversion set-up and assimilated data on posterior uncertainties in CH_4 emissions the Carbon Tracker Europe – CH4 (CTE-CH4) atmospheric inversion model was used with both in situ and TROPOMI observations. The results indicate the potential of the TROPOMI data to better separate wetland and anthropogenic emissions, as well as to constrain spatial distributions. The length of the assimilation window and prior flux uncertainties have a significant impact on the optimised regional fluxes, in particular the distribution between biospheric and anthropogenic emissions, and on the seasonality in posterior fluxes. The length of the assimilation window needs to be chosen depending on the set-up of the inversion and number of assimilated data on different temporal and spatial domains

Using the LOTOS-EUROS simulation model in forward mode with an ensemble of realistic emission inventories only occasionally the specified uncertainty in fossil fuel emissions is able to explain the difference between simulations and observations at some of the ICOS sites. This suggests that the uncertainties in emissions that are usually assumed in inversion systems are higher than what is specified in the current emission uncertainty parameterization in the TNO/GHGco v4.0 European emission inventory.

For a more comprehensive summary of the analysis of the individual results, we forward the reader to the individual conclusion sections above (Section 2 for CCFFDAS operated by iLab/ULUND, Section 3 for CTE-CH4 operated by FMI, Section 4 for the Western Europe analytical inversion system operated by LSCE, and Section 5 for LOTOS-EUROS operated

by TNO). However, as a final note, all presented work highlight the required complexity in the design of the modelling systems that link atmospheric tracers to posterior uncertainties in the CO_2 fossil fuel emissions. Therefore, the results emphasize the importance of quantifying and taking into account all aspects of the design options and prior specifications for the CO_2 emissions Monitoring and Verification Support capacity.

7 References

Asefi-Najafabady, S., Rayner, P. J., Gurney, K. R., McRobert, A., Song, Y., Coltin, K., Huang, J., Elvidge, C., and Baugh, K. (2014), A multiyear, global gridded fossil fuel CO_2 emission data product: Evaluation and analysis of results, *J. Geophys. Res. Atmos.*, 119, 10,213– 10,231, doi:10.1002/2013JD021296.

Balsamo, Gianpaolo, Richard Engelen, Daniel Thiemert, Anna Agusti-Panareda, Nicolas Bousserez, Grégoire Broquet, Dominik Brunner, et al. 2021. The CO2 Human Emissions (CHE) Project: First Steps Towards a European Operational Capacity to Monitor Anthropogenic CO2 Emissions. *Frontiers in Remote Sensing* 2. https://www.frontiersin.org/articles/10.3389/frsen.2021.707247.

Buchwitz, M., Reuter, M., Bovensmann, H., Pillai, D., Heymann, J., Schneising, O., et al. (2013). Carbon Monitoring Satellite (CarbonSat): Assessment of Atmospheric CO2 and CH4 Retrieval Errors by Error Parameterization. Atmos. Meas. Tech. 6, 3477–3500. Available at: https://www.atmos-meas-tech.net/6/3477/2013/. doi:10.5194/amt-6-3477-2013

Evensen, G., 2003. The Ensemble Kalman Filter: theoretical formulation and practical implementation. Ocean Dynamics 53, 343–367. https://doi.org/10.1007/s10236-003-0036-9

Crippa, M.; Solazzo, E.; Huang, G.; Guizzardi, D.; Koffi, E.; Muntean, M.; Schieberle, C.; Friedrich, R.; Janssens-Maenhout, G. High resolution temporal profiles in the Emissions Database for Global Atmospheric Research. Sci. Data **2020**, 7, 121.EDGARv6.0. Available online: https://edgar.jrc.ec.europa.eu/index.php/dataset_ghg60

Etiope, G.; Ciotoli, G.; Schwietzke, S.; Schoell, M. Gridded maps of geological methane emissions and their isotopic signature. Earth Syst. Sci. Data **2019**, 11, 1–22.

Giglio, L.; Randerson, J.T.; van derWerf, G.R. Analysis of daily, monthly, and annual burned area using the fourth-generation global fire emissions database (GFED4). J. Geophys. Res. Biogeosci. **2013**, 118, 317–328.

Hascoët, L.L., Pascual, V.V., 2013. The Tapenade Automatic Differentiation tool: principles, model, and specification. ACM Trans. Math. Softw. 39 (3).

Heimann, M., and S. Körner, (2003), The global atmospheric tracer model TM3, Tech. Rep. 5, Max-Planck-Institut für Biogeochemie, Jena, Germany.

Hersbach, H, Bell, B, Berrisford, P, et al. The ERA5 global reanalysis. *Q J R Meteorol Soc*. 2020; 146: 1999– 2049. https://doi.org/10.1002/qj.3803

Houweling, S.; Bergamaschi, P.; Chevallier, F.; Heimann, M.; Kaminski, T.; Krol, M.; Michalak, A.M.; Patra, P. Global inverse modeling of CH4 sources and sinks: An overview of methods. Atmos. Chem. Phys. 2017, 17, 235–256.

Ito, A., Hajima, T., Lawrence, D.M., Brovkin, V., Delire, C., Guenet, B., Jones, C.D., Malyshev, S., Materia, S., McDermid, S.P., Peano, D., Pongratz, J., Robertson, E., Shevliakova, E., Vuichard, N., Wårlind, D., Wiltshire, A., Ziehn, T., 2020. Soil carbon sequestration simulated in CMIP6-LUMIP models: implications for climatic mitigation. Environ. Res. Lett. 15, 124061. https://doi.org/10.1088/1748-9326/abc912

Kaminski, T., W. Knorr, P. Rayner, and M. Heimann (2002), Assimilating atmospheric data into a terrestrial biosphere model: A case study of the seasonal cycle, Global Biogeochem. Cycles, 16(4), 14-1–14-16, doi:10.1029/2001GB001463.

Kaminski, T., Scholze, M., Voßbeck, M., Knorr, W., Buchwitz, M., and Reuter, M.: Constraining a terrestrial biosphere model with remotely sensed atmospheric carbon dioxide, Remote Sensing of Environment, pp. 109 – 124, https://doi.org/http://dx.doi.org/10.1016/j.rse.2017.08.017, URL http://www.sciencedirect.com/science/article/pii/S0034425717303838, 2017.

Kaminski, Thomas, and Peter Julian Rayner. 2017. Reviews and Syntheses: Guiding the Evolution of the Observing System for the Carbon Cycle through Quantitative Network Design. *Biogeosciences* 14 (20): 4755-66. https://doi.org/10.5194/bg-14-4755-2017.

Kaminski, Thomas, Marko Scholze, Peter Rayner, Sander Houweling, Michael Voßbeck, Jeremy Silver, Srijana Lama, et al. 2022b. Assessing the Impact of Atmospheric CO2 and NO2 Measurements From Space on Estimating City-Scale Fossil Fuel CO2 Emissions in a Data Assimilation System. *Frontiers in Remote Sensing* 3. https://www.frontiersin.org/articles/10.3389/frsen.2022.887456.

Kaminski, T., Scholze, M., Rayner, P., Voßbeck, M., Buchwitz, M., Reuter, M., Knorr, W., Chen, H., Agustí-Panareda, A., Löscher, A., and Meijer, Y.: Assimilation of atmospheric CO2 observations from space can support national CO2 emission inventories, Environmental Research Letters, 17, 014 015, https://doi.org/10.1088/1748-9326/ac3cea, URL https://doi.org/10.1088/1748-9326/ac3cea, 2022.

Krol, M., Houweling, S., Bregman, B., van den Broek, M., Segers, A., van Velthoven, P., Peters, W., Dentener, F., Bergamaschi, P., 2005. The two-way nested global chemistry-transport zoom model TM5: algorithm and applications. Atmospheric Chemistry and Physics 5, 417–432. https://doi.org/10.5194/acp-5-417-2005

Knorr, Wolfgang, and Martin Heimann. 1995. Impact of drought stress and other factors on seasonal land biosphere CO2 exchange studied through an atmospheric tracer transport model. *Tellus B: Chemical and Physical Meteorology* 47 (4): 471-89. https://doi.org/10.3402/tellusb.v47i4.16062.

Lespinas, F., Wang, Y., Broquet, G., Bréon, F.-M., Buchwitz, M., Reuter, M., Meijer, Y., Loescher, A., Janssens-Maenhout, G., Zheng, B., and Ciais, P.: The potential of a constellation of low earth orbit satellite imagers to monitor worldwide fossil fuel CO2 emissions from large cities and point sources, Carbon Balance and Management, 15, 18, https://doi.org/10.1186/s13021-020-00153-4, 2020.

Lienert, S., Joos, F., 2018. A Bayesian ensemble data assimilation to constrain model parameters and land-use carbon emissions. Biogeosciences 15, 2909–2930. https://doi.org/10.5194/bg-15-2909-2018

Lorente, A.; Borsdorff, T.; Butz, A.; Hasekamp, O.; aan de Brugh, J.; Schneider, A.; Wu, L.; Hase, F.; Kivi, R.; Wunch, D.; et al. Methane retrieved from TROPOMI: Improvement of the data product and validation of the first 2 years of measurements. Atmos.Meas. Tech. 2021, 14, 665–684.

Lorente, A., K. F. Boersma, H. J. Eskes, J. P. Veefkind, J. H. G. M. van Geffen, M. B. de Zeeuw, H. a. C. Denier van der Gon, S. Beirle, et M. C. Krol. 2019. Quantification of Nitrogen Oxides Emissions from Build-up of Pollution over Paris with TROPOMI. *Scientific Reports* 9 (1): 20033. https://doi.org/10.1038/s41598-019-56428-5.

Manders, A. M. M., Builtjes, P. J. H., Curier, L., Denier van der Gon, H. A. C., Hendriks, C., Jonkers, S., Kranenburg, R., Kuenen, J. J. P., Segers, A. J., Timmermans, R. M. A., Visschedijk, A. J. H., Wichink Kruit, R. J., van Pul, W. A. J., Sauter, F. J., van der Swaluw, E., Swart, D. P. J., Douros, J., Eskes, H., van Meijgaard, E., van Ulft, B., van Velthoven, P.,

Banzhaf, S., Mues, A. C., Stern, R., Fu, G., Lu, S., Heemink, A., van Velzen, N., and Schaap, M.: Curriculum vitae of the LOTOS–EUROS (v2.0) chemistry transport model, Geosci. Model Dev., 10, 4145-4173, https://www.geosci-model-dev.net/10/4145/2017/

Marshall, J., Nuñez Ramirez, T., and partners, W. C.: Attribution Problem Configurations, CO2 Human Emissions, H2020 European Project, https://www.che-project.eu/sites/default/files/2020-01/CHE-D4-3-V4-1.pdf, 2019

Menut, L., Bessagnet, B., Khvorostyanov, D., Beekmann, M., Blond, N., Colette, A., Coll, I., Curci, G., Foret, G., Hodzic, A., Mailler, S., Meleux, F., Monge, J.-L., Pison, I., Siour, G., Turquety, S., Valari, M., Vautard, R., and Vivanco, M. G.: CHIMERE 2013: a model for regional atmospheric composition modelling, Geoscientific Model Development, 6, 981–1028, https://doi.org/10.5194/gmd-6-981-2013, 2013.

Nakicenovic, N.: Socioeconomic driving forces of emissions scenarios, in: The global carbon cycle: Integrating humans, climate, and the natural world, edited by Field, C. B. and Raupach, M. R., pp. 225–239, Island Press, Washington, D.C., 2004.

Peters, W.; Miller, J.B.; Whitaker, J.; Denning, A.S.; Hirsch, A.; Krol, M.C.; Zupanski, D.; Bruhwiler, L.; Tans, P.P. An ensemble data assimilation system to estimate CO2 surface fluxes from atmospheric trace gas observations. J. Geophys. Res. 2005, 110, D24304.

Pinty, B., Clerici, M., Andredakis, I., Kaminski, T., Taberner, M., Verstraete, M. M., Gobron, N., Plummer, S., and Widlowski, J.-L.: Exploiting the MODIS albedos with the Two-stream Inversion Package (JRC-TIP): 2. Fractions of transmitted and absorbed fluxes in the vegetation and soil layers, Journal of Geophysical Research – Atmospheres, 116, D09 106, https://doi.org/10.1029/2010JD015373, 2011.

Potier, E., Broquet, G., Wang, Y., Santaren, D., Berchet, A., Pison, I., Marshall, J., Ciais, P., Bréon, F.-M., and Chevallier, F.: Complementing XCO2 imagery with ground-based CO2 and 14CO2 measurements to monitor CO2 emissions from fossil fuels on a regional to local scale, Atmos. Meas. Tech., 15, 5261–5288, https://doi.org/10.5194/amt-15-5261-2022, 2022.

Rayner, Peter J., Anna M. Michalak, and Frédéric Chevallier. 2019. Fundamentals of Data Assimilation Applied to Biogeochemistry. *Atmospheric Chemistry and Physics* 19 (22): 13911-32. https://doi.org/10.5194/acp-19-13911-2019.

Skamarock, C., B. Klemp, Jimy Dudhia, O. Gill, Dale Barker, G. Duda, Xiang-yu Huang, Wei Wang, et G. Powers. 2008. « A Description of the Advanced Research WRF Version 3 ». https://doi.org/10.5065/D68S4MVH.

Saunois, M.; Stavert, A.R.; Poulter, B.; Bousquet, P.; Canadell, J.G.; Jackson, R.B.; Raymond, P.A.; Dlugokencky, E.J.; Houweling, S.; Patra, P.K.; et al. The Global Methane Budget 2000–2017. Earth Syst. Sci. Data 2020, 12, 1561–1623.

Super, Ingrid, Stijn N. C. Dellaert, Antoon J. H. Visschedijk, et Hugo A. C. Denier van der Gon. 2020. « Uncertainty Analysis of a European High-Resolution Emission Inventory of CO_2 and CO to Support Inverse Modelling and Network Design ». *Atmospheric Chemistry and Physics* 20 (3): 1795-1816. https://doi.org/10.5194/acp-20-1795-2020.

Super, I.; Scarpelli, T.; Droste, A.; Palmer, P.I., 2023: Improved definition of prior uncertainties in CO_2 and CO fossil fuel fluxes and the impact on a multi-species inversion. Atmos. Chem. Phys., *Submitted.*

Tarantola, Albert. 2005. *Inverse Problem Theory and Methods for Model Parameter Estimation*. Other Titles in Applied Mathematics. Society for Industrial and Applied Mathematics. https://doi.org/10.1137/1.9780898717921.

Tsuruta, A., Aalto, T., Backman, L., Hakkarainen, J., van der Laan-Luijkx, I.T., Krol, M.C., Spahni, R., Houweling, S., Laine, M., Dlugokencky, E., Gomez-Pelaez, A.J., van der Schoot, M., Langenfelds, R., Ellul, R., Arduini, J., Apadula, F., Gerbig, C., Feist, D.G., Kivi, R., Yoshida, Y., Peters, W., 2017. Global methane emission estimates for 2000–2012 from CarbonTracker Europe-CH4 v1.0. Geoscientific Model Development 10, 1261–1289. https://doi.org/10.5194/gmd-10-1261-2017

Tsuruta, A., Kivimäki, E., Lindqvist, H., Karppinen, T., Backman, L., Hakkarainen, J., Schneising, O., Buchwitz, M., Lan, X., Kivi, R., Chen, H., Buschmann, M., Herkommer, B., Notholt, J., Roehl, C., Té, Y., Wunch, D., Tamminen, J., Aalto, T., 2023. CH4 Fluxes Derived from Assimilation of TROPOMI XCH4 in CarbonTracker Europe-CH4: Evaluation of Seasonality and Spatial Distribution in the Northern High Latitudes. Remote Sensing 15, 1620. https://doi.org/10.3390/rs15061620

US EPA Office of Research and Development (2018): CMAQ. doi:10. 5281/zenodo.1212601 Available at: https://www.frontiersin.org/articles/10. 3389/frsen.2021.689838/full#B13.

Wang, Y., Broquet, G., Ciais, P., Chevallier, F., Vogel, F., Wu, L., Yin, Y., Wang, R., and Tao, S.: Potential of European $^{14}CO_2$ observation network to estimate the fossil fuel CO_2 emissions via atmospheric inversions, Atmos. Chem. Phys., 18, 4229–4250, https://doi.org/10.5194/acp-18-4229-2018, 2018.

Weber, T.; Wiseman, N.A.; Kock, A. Global ocean methane emissions dominated by shallow coastal waters. Nat. Commun. **2019**, 10, 4584.

Document History

Version	Author(s)	Date	Changes
Draft 1	all	04/08/2023	Initial Version
Draft 2	T. Kaminski	24/08/2023	edits section 5 suggested by TNO team
Final V1-0	T. Kaminski	26/09/2023	edits after internal review

Internal Review History

Internal Reviewers	Date	Comments
Marc Guevara Vilardell (BSC)	18/09/2023	Suggested a few comments/corrections
Elena Saltikoff and Sindu Raj Parampil (ICOS)	19/09/2023	"Congratulations, the deliverable reads well and it is educational even for those who are not so deeply involved in data assimilation." Suggested comments.

Estimated Effort Contribution per Partner

Partner	Effort
iLab (lead)	9 PM
FMI	4 PM
LSCE	1 PM
MPG	0.5 PM
TNO	3 PM
ULund	
Total	